



UNIVERSITY OF LEEDS

This is a repository copy of *Ti6Al4V metal cutting chip formation experiments and modelling over a wide range of cutting speeds*.

White Rose Research Online URL for this paper:  
<http://eprints.whiterose.ac.uk/126440/>

Version: Accepted Version

---

**Article:**

Childs, THC, Arrazola, P-J, Aristimuno, P et al. (2 more authors) (2018) Ti6Al4V metal cutting chip formation experiments and modelling over a wide range of cutting speeds. *Journal of Materials Processing Technology*, 255. pp. 898-913. ISSN 0924-0136

<https://doi.org/10.1016/j.jmatprotec.2018.01.026>

---

Copyright (c) 2018 B. V. Licensed under the Creative Commons Attribution-Non Commercial No Derivatives 4.0 International License (<https://creativecommons.org/licenses/by-nc-nd/4.0/>)

**Reuse**

This article is distributed under the terms of the Creative Commons Attribution-NonCommercial-NoDerivs (CC BY-NC-ND) licence. This licence only allows you to download this work and share it with others as long as you credit the authors, but you can't change the article in any way or use it commercially. More information and the full terms of the licence here: <https://creativecommons.org/licenses/>

**Takedown**

If you consider content in White Rose Research Online to be in breach of UK law, please notify us by emailing [eprints@whiterose.ac.uk](mailto:eprints@whiterose.ac.uk) including the URL of the record and the reason for the withdrawal request.



[eprints@whiterose.ac.uk](mailto:eprints@whiterose.ac.uk)  
<https://eprints.whiterose.ac.uk/>

# Ti6Al4V METAL CUTTING CHIP FORMATION EXPERIMENTS AND MODELLING OVER A WIDE RANGE OF CUTTING SPEEDS

Thomas H.C. Childs<sup>a\*</sup>, Pedro-J. Arrazola<sup>b</sup>, P. Aristimuno<sup>b</sup>, Ainhara Garay<sup>b</sup>, Irantzu Sacristan<sup>b</sup>

<sup>a</sup>: School of Mechanical Engineering, University of Leeds, Leeds LS29JT, UK

<sup>b</sup>: Faculty of Engineering, Mondragon University, Mondragon 20500, Spain

**Abstract.** Measured forces, chip geometry and tool temperatures from machining a mill annealed Ti6Al4V at cutting speeds mainly from 1 to 100 m/min, but in some cases down to 0.1 m/min, are reported, as well as mechanical testing of the material. Finite element simulations with inputs the measured flow stress, and subsequently a small high temperature strain hardening recovery correction, and a failure model calibrated from the cutting tests at speeds from 1 to 10 m/min, give satisfactory agreement with the higher speed tests once surface strain hardening and damage from the previous pass of the tool are taken into account. This paper's originality is firstly to show that more complicated flow stress models involving large strain softening are not needed provided shear failure is included; and secondly its failure model: this proposes a non-zero failed shear stress depending on local pressure and temperature. The simulations provide relations between tool mechanical and thermal loading and cutting conditions to aid process improvement.

**Keywords:** Flow and failure modelling; Force and temperature measurement; Serrated chips.

## 1. Introduction

Attempts to predict the occurrence of localised shear or segmented chip formation in metal cutting, that gives rise to saw-tooth chip shapes, and the cutting forces, tool stresses and temperatures associated with that, have been a continuing activity for the past 50 years. One reason is that difficult-to-machine metals such as titanium alloys, nickel super-alloys and hardened steels show this type of chip formation at industrially used cutting speeds and feeds. Of these, the titanium alloy Ti6Al4V has the longest history of study.

Adiabatic heating is a common but not the only cause of localised shear. Ti6Al4V also shows segmented chips, though less serrated than saw teeth, in non-adiabatic conditions. Evidence for the importance of adiabatic conditions comes from observations that saw tooth chips occur above minimum values of the product  $hv_c$ , with  $h$  the uncut chip thickness and  $v_c$  the cutting speed. When  $hv_c$  is non-dimensionalised by the chip material's thermal diffusivity  $\kappa$ , the minimum value of  $hv_c/\kappa$ , which has the physical meaning of a Peclet number, is found to lie in a narrow range from  $\approx 20$  to 50 (Table 1). Above this range heat flow by conduction during chip formation is negligible, i.e. conditions are adiabatic.

**Table 1**  
Minimum values of  $hv_c$  and of  $hv_c/\kappa$  for saw tooth chip formation, from (Childs, 2014).

Metal alloy	$(hv_c)_{\min}$ (mm <sup>2</sup> /s)	$(hv_c)_{\min}/\kappa$
Ti6Al4V	70 – 150	20 – 40
Inconel 718	100 – 170	30 – 50
AISI 1045 steel: Q&T HRC50	300 - 330	20 - 22
Q&T HRC30	430 – 480	29 – 32

As  $hv_c$  increases towards adiabatic conditions, the temperature rise in the chip formation zone, due to plastic work, increases. The transition to saw tooth chip formation was considered in early theories to be due to increased thermal softening, that encourages shear localisation, overcoming strain hardening acting against it. Theories focussed on a criterion

for localisation and how to calculate the temperature. Recht (1964) estimated temperature in the case that the shear had just localised. He proposed that the localisation would continue catastrophically if, at that instant, the thermal softening equalled or just exceeded the strain hardening. He successfully ranked alloys according to their relative transition cutting speeds but was not able to give absolute values to those speeds. Semiatin and Rao (1983) calculated temperature in the primary shear zone before the transition. They proposed that localisation required the thermal softening at transition to be significantly larger than the strain (and strain-rate) hardening by a factor in accord with experience from other high-speed forming processes. They were able to give absolute values to transition cutting speeds, based on this experience factor. In contrast Hou and Komanduri (1997) argued that all that was needed for localisation was that the combined effects of strain and temperature should reduce flow stress within the primary shear zone to less than its pre-flow value. They put their effort into a temperature calculation much more detailed than that by Semiatin and Rao, also successfully to predict transition cutting speed.

None of these three influential and well-received papers consider the possibility that the hydrostatic pressure distribution as well as the flow stress distribution within the chip formation zone should affect localisation and that the pressure distribution would be changed by thermal softening, despite Oxley's earlier work that shows that pressure distribution is altered by strain hardening (Oxley and Welsh, 1963, in Oxley, 1989). Nor do they consider possible destabilization due to micro-voiding and strain softening, the pre-cursor to ductile shear failure, though Hou and Komanduri acknowledge it, only to disregard it, while in earlier work Komanduri argues for crack formation at low cutting speeds (Komanduri and von Turkovich, 1981) and in contemporary work Shaw makes the case for cracking as the cause of serration (Vyas and Shaw, 1999). All three works pre-date the development of finite element chip formation simulations which, in principle, make redundant the need for a

localisation criterion. Localisation should emerge naturally from the input material properties and machining parameters. It is now clear from such simulations, certainly for Ti alloys, that some form of strain softening (or failure law) is necessary to account for chip formation with the severe level of instability that merits the description of chips as saw-tooth shaped.

An early well-founded simulation by Calamaz et al. (2008), without strain softening or a failure law, shows segmented chip formation of Ti6Al4V when  $h v_c = 300 \text{ mm}^2/\text{s}$  ( $h = 0.1 \text{ mm}$ ,  $v_c = 180 \text{ m/min}$ ) but the segment shape is far from that observed in experiments. There is no segmentation when  $h v_c = 100 \text{ mm}^2/\text{s}$  although experiments show that there should be. The simulations' flow stress dependence on strain, strain rate and temperature is in the form of a Johnson-Cook model with its coefficients obtained in a standard way from split Hopkinson bar testing. Calamaz et al., with an improved treatment in (Calamaz et al., 2010), achieve more realistic chip shapes, at high and low values of  $h v_c$ , by modifying the Johnson-Cook model so that strain hardening gives way to strain softening at temperatures greater than  $\approx 300^\circ\text{C}$  and strains greater than  $\approx 0.7$  (i.e. beyond the range of the Hopkinson bar testing). They justify this as due to dynamic recovery / recrystallization. The strain softening reduces the flow stress to  $\sim$  half its value in the absence of softening, as strains increase above 1. More recently Liu et al. (2013) introduced a combined softening and failure model. Recovery sets in at a strain  $\approx 1$ . In addition partial shear failure initiates at a strain  $\approx 0.3$  to 0.5, also eventually reducing flow stress to  $\sim$  half its value in the absence of softening, at strains in the range 1 to 1.5. The failure strain, though, is a function of strain-rate and not of hydrostatic pressure and temperature (as is proposed in this paper, in Section 3). Most recently the same group (Melkote et al., 2015) has developed a strain softening flow stress model from first principles, considering grain refinement during shear, for commercially pure Ti. It predicts saw-tooth chip formation with strain softening setting in at strains  $\approx 0.4$  to 0.5

in the temperature and strain rate conditions of machining. They comment that a better simulation would include a ductile failure criterion.

A well-known form of ductile failure law (Eq. 1) expresses that damage  $D$  accumulates along a material's equivalent strain path, depending on the variation of failure strain  $\bar{\varepsilon}_f$  along the path.  $\bar{\varepsilon}_f$  is the product of  $\varepsilon_{f,0}$ , the failure strain in simple shear / torsion, and  $\exp(c\eta)$ .  $c$  is a negative constant and  $\eta$ , the stress triaxiality, is the ratio of hydrostatic stress  $\sigma_m$  to the material's flow stress  $\bar{\sigma}$ . Any dependence of  $\bar{\varepsilon}_f$  on temperature and strain rate is included within  $\varepsilon_{f,0}$ . Failure occurs as  $D \Rightarrow 1$ .

$$D = \int_{\text{path}} \frac{d\bar{\varepsilon}}{\bar{\varepsilon}_f}; \quad \text{failure as } D \Rightarrow 1.0 \quad (1)$$

$$\bar{\varepsilon}_f = \varepsilon_{f,0} \exp(c\eta)$$

Simulations of Ti6Al4V machining that include a failure law of this type realistically predict serrated chip formation (for example Chen et al., 2011). The opposite problem to ignoring strain-softening in the absence of a failure model must be overcome. The flow stress at failure must be prevented from falling to zero. Ways of doing this, failure mitigation as it were, with catastrophic consequences of not doing so, are illustrated in (Liu et al., 2014).

An uncertainty in much of the modelling / simulation literature is that material flow and failure data are assumed from other work. When experiments are carried out (and when experimental results are taken from other work too) it is by no means certain that the flow and failure data match the properties of the actually machined materials. For example Calamaz et al. (2010) assume a linear thermal softening of Ti6Al4V, i.e.  $m = 1$  in the Johnson-Cook (1985) flow stress model, although there is a substantial literature that shows flow stress decreasing concave downwards with increasing temperature, i.e.  $m < 1$ . Liu et al (2014) take, in Eq. 1,  $\varepsilon_{f,0} = 0.25$  at low strain-rate and room temperature and  $c = -0.5$ . These

values can be traced back to Johnson and Holmquist (1989). Other authors use these values too. It is now understood (for example Bai and Wierzicki, 2010) that failure strain depends on the third stress invariant as well as on  $\eta$  (with differing importance for different alloys). Historical values of  $\varepsilon_{f,0}$ ,  $c$  may not be correct for plane strain modelling if they were obtained from the failure of axially symmetric test pieces. Recent work (Allahverdizadeh et al., 2015) on annealed Ti6Al4V that takes this into account gives for plain strain conditions, after manipulation of its data to the form of Eq. 1,  $\varepsilon_{f,0} = 0.51$  and  $c = -0.43$ . Other recent work gives  $\varepsilon_{f,0} = 0.37$  and  $c = -0.15$  (Hammer, 2012), although (Simha and Williams, 2016) give  $\varepsilon_{f,0} = 0.5$  and  $c = -1.4$  based on the same data. For steels,  $c$  is found in the range  $-0.5$  to  $-2.5$  in plane strain conditions (Childs, 2013). It is an open question what are the appropriate values of  $\varepsilon_{f,0}$  and  $c$  for Ti6Al4V particularly for the compressive conditions existing in the shear region of metal cutting chip formation.

A further issue with much of the literature is selection of the sliding friction contact condition between the chip and tool. It is recognized that contact stresses are high so that the contact is divided into a region close to the cutting edge where friction stress is close to the shear flow stress of the chip material, and a region further from the edge where friction stress is some fraction  $\mu$  (the friction coefficient) of the normal stress. But usually  $\mu$  is chosen to give good agreement between the ratio of thrust and cutting forces. For example, Melkote et al. (2015) apply different values of  $\mu$ , from 0.27 to 0.63, to each of the 15 conditions that they simulate.

A final issue is that as material flow and failure models become more complicated it becomes more difficult to determine their critical features that control the outcomes of simulations based on them.

The present paper combines modelling and simulation with experimental work. It includes flow stress and failure characterisation of the actual experimental material although

it has been necessary to extrapolate the range of the characterisation by reference to and matching with previous works. It develops equations to describe the actual flow stress and failure behaviours rather than fitting the behaviours to existing equations; and it keeps various adjustable parameters to the smallest number possible in order better to assess which are critical to predictions. It applies a default friction coefficient  $\mu = 1$ , based on previous experience that such a high value forces the contact into the, realistic, high stress regime in which friction stress equals shear flow stress over a greater part of the chip / tool contact length (Childs and Rahmad, 2010).

The paper's hypothesis is that it is not necessary to invoke a major strain softening to account for observed chip formation (although a small adjustment for recovery is found to improve agreement between simulations and experiments). Instead, ductile shear failure initiates unstable flow. Its novel feature concerns the flow stress at failure. It is taken to be a fraction of the unfailed flow stress, with the fraction varying from 0 to 1 depending on the stress triaxiality and temperature. It is a development from earlier work considering only stress triaxiality dependence that successfully predicts built up edge formation in the machining of steels (Childs, 2013).

Two groups of machining experiments have been carried out. In the first group, the uncut chip thickness  $h$  and cutting speed  $v_c$  are in the ranges 0.05 to 0.25 mm and 0.1 to 30 m/min. The product  $hv_c < 50 \text{ mm}^2/\text{s}$  in all cases except for the largest combinations of  $h$  and  $v_c$ . For  $hv_c < 50 \text{ mm}^2/\text{s}$  shear localisation is not adiabatic but due to shear failure (Table 1). The purpose of this group of experiments is to validate and calibrate the shear failure model. It is found that the cutting speed range  $v_c$  from 1 to 10 m/min is most useful for this. In the second group  $h$  is from 0.1 to 0.4 mm and  $v_c$  from 40 to 100 m/min. These are the industrially used conditions. The experimentally measured cutting and thrust forces, tool rake temperatures and chip shapes are compared with predictions from simulations with inputs of

the experimentally determined flow stress behaviour of the Ti6Al4V and the failure behaviour validated in the first group of experiments. Agreement is found between experimental and predicted forces and temperatures. To obtain agreement between simulated and experimental chip shapes it is additionally necessary to consider the damage and strain created in the cut surface by the previous pass of the tool.

## 2. Experimentation

All of the work material characterisation and the first group of cutting tests (low  $h_{vc}$ , non-adiabatic to calibrate the shear failure model) and some of the second group of tests (high  $h_{vc}$ , industrially used) have been carried out on a single as-received billet, billet A, of Ti6Al4V, 400 mm long and 290 mm diameter. The high  $h_{vc}$  test results are augmented by recent pre-existing but previously unpublished results from two further billets B and C. All three billets are from the same supplier and of the same grade, with the same as-received heat treatment: mill annealed at 750°C for 2h and air cooled. The composition of billet A from four measurements at different positions is  $6.5 \pm 0.1$  wt% Al,  $4.1 \pm 0.1$  wt% V,  $1880 \pm 110$  ppm O, balance Ti.

Fig. 1 shows similar chip microstructures from all three billets. Microstructure between serrations is similar to that of as-received material, which is bi-modal, formed by globular primary  $\alpha$  phase (white in the image) and acicular  $\alpha$  phase contained in a transformed  $\beta$  matrix (black in the image). The primary  $\alpha$  grain size is  $G = 8$  (ASTM, 2013) and accounts for 70% by volume of the alloy. Fig. 1 also shows qualitatively the different chip shapes from low and high  $h_{vc}$  tests. The serrations from billet A at low  $h_{vc}$  ( $1.7 \text{ mm}^2/\text{s}$ ) are less pronounced and more irregular than those from billets B and C at high  $h_{vc}$ .

(respectively 170 and 270 mm<sup>2</sup>/s). The chip serration dimensions  $t_{max}$  and  $t_{min}$  are defined on billet C, for later use.

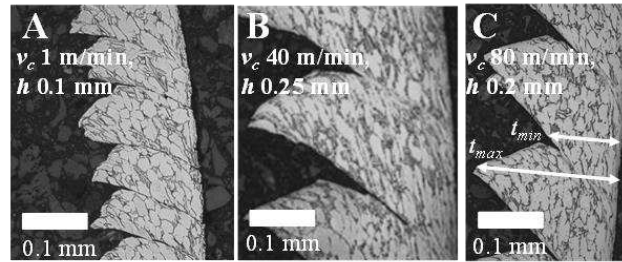


**Fig. 1.** Billet A to C microstructures observed in chip sections. The less pronounced chip serration at low  $h v_c$  (billet A) is also seen.

## 2.1. Flow stress and failure determination

Large amounts of data exist in the literature on the flow stress dependence of Ti6Al4V on strain, strain rate and temperature. The flow stress behaviour of billet A material has been measured to place it amongst this data and partially to validate the flow stress model to be used here.

Strain hardening at  $\approx 25^\circ\text{C}$  and a strain rate of  $\approx 10^{-3}/\text{s}$  has been measured by plane strain compression testing. The Ti6Al4V strip, cut transversely from the billet to give a longitudinal compression direction, was 1.5 mm thick, 18 mm wide and  $> 20$  mm long. The plane strain compression dies, overlapping the strip in the width direction, were 3 mm wide. Loading was incremental with lubrication between increments by re-application of a PTFE tape at the die / strip contact. Testing was repeated three times (with three strips). These tests also gave information on shear failure. Load was applied up to the first instance of cracking of the sample. This was by shear and localised at the opposite edges of the 18 mm width. Side spread of the sample there indicated that the stress state was closer to uniaxial compression than plane strain, i.e. triaxiality  $\eta \approx - 1/3$ .

Temperature and strain rate dependence of flow stress have been measured by simple compression of cylinders 12 mm high and 8 mm diameter. They were cut from the billet to give axes in the longitudinal direction. All tests were repeated at least twice. Quasi-static, ambient temperature tests used a 100kN Instron test machine. Loading was incremental with PTFE tape lubrication. Elevated temperature and medium strain rate tests were carried out continuously in a Gleeble 3500 hydraulic test machine. Testing was in vacuum with graphite lubrication, after heating at a rate of 10°C/s and holding for 20s, as in (Iturbe et al., 2017). Testing was at temperatures of 25 to 800°C at a strain rate of 1/s, at 400 to 800°C at 10/s and at 800°C at 100/s. Testing at a higher strain rate, for example by split Hopkinson bar testing, was not available for this project.

## 2.2. Low speed cutting tests

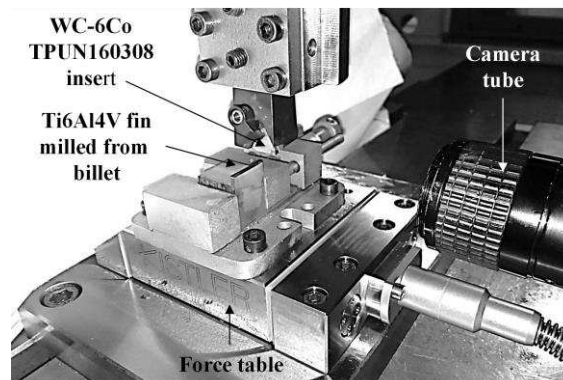
Orthogonal planing has been carried out dry, with  $v_c$  from 0.1 to 30 m/min and  $h$  from 0.05 to 0.5 mm. Plane rake face WC-6Co (H13A) inserts of 5° rake and 6° clearance angle have been used. Their measured edge radius  $r_\beta$  was 8 to 12  $\mu\text{m}$ .

Fig. 2 shows a detail of the set up. The planing has been of a 2 mm wide, 20 mm long, fin milled from a cuboid cut from billet A. The billet is clamped on a Kistler 9129AA force platform which in turn is bolted to the table of a vertical CNC milling machine. The table provides the cutting speed motion. The insert in its holder is held on the non-rotating spindle of the milling machine. The mass and stiffness of the insert support give it a resonant frequency of 160 Hz in the cutting direction and 150 Hz in the thrust direction, as obtained by a hammer impact test, measuring the insert vibration with a laser displacement meter (resolution 0.01  $\mu\text{m}$ ).

A high speed video camera (Photron FASTCAM APX RS) views the cutting from the side at a frame rate of 1,500 to 10,000/s. Frames and the cutting and thrust force ( $F_C$  and  $F_T$ )

outputs from the Kistler (sampled at 10 times frame rate) are synchronised and recorded. Fig. 3 is an example of one frame output. A cursor identifies the force state at the instant of the frame.

Chips collected after a test are sectioned and polished to obtain the maximum and minimum chip thicknesses  $t_{\max}$  and  $t_{\min}$ , defined in Fig. 1.



**Fig. 2.** The low speed cutting set up.

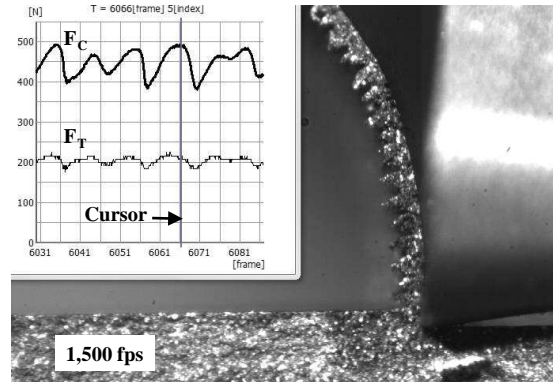


**Fig. 3.** Force and video output example:  $v_c = 1$  m/min,  $h = 0.05$  mm.

### 2.3. Higher speed cutting tests

Orthogonal dry cutting has been carried out, with additional data provided from pre-existing semi-orthogonal and flood cooled tests, all with  $v_c$  from 40 to 100 m/min and  $h$  from 0.1 to 0.4 mm, and all with uncoated H13A inserts of rake angle 5 to 7°. In contrast to the low speed tests,  $r_\beta$  has been measured in the range 30 to 40  $\mu\text{m}$ .

Orthogonal cutting has reduced the length of tube. Tube of wall thickness 2 mm was machined from billet A and mounted in the spindle of a vertical CNC milling machine. The cutting insert in its holder was bolted to a Kistler force platform on the stationary table of the machine. Cutting speed and feed were generated by the spindle's rotation and axial feed. Machining was dry. Forces were recorded and chips collected, sectioned and polished.

Pre-existing orthogonal cutting of billet B was with the same set up, with the addition that the side face of the cutting insert was ground normal to the cutting edge and overhung the tube wall by  $\approx 0.3$  mm. In addition to force and chip measurement, the temperature distribution on the tool side face was obtained by infra-red imaging. Detail of the set up and method has been published before (Armendia et al., 2010).

Force and chip measurements also pre-existed for orthogonal cutting of billet C. In that case tube of 5 mm wall thickness was obtained from the billet and turned on a lathe in flood coolant conditions.

Semi-orthogonal cutting has been turning of bar from billets A and C in a horizontal CNC lathe with flood coolant and with tools of nose radius 0.8 and 1.6 mm and cutting edge engagement length 4 to 5 mm.

### **3. Models and simulation conditions**

This paper's flow stress, failure and chip / tool friction models are given here. The simulation conditions are also presented. General simulation results of the features of chip formation are in Section 4: how field variables such as damage, stress triaxility, temperature and strain vary with cut distance,  $h$  and  $v_c$ . Quantitative predictions of  $F_C$ ,  $F_T$ ,  $t_{\max}$  and  $t_{\min}$  and of maximum tool temperature, and further chip formation views, are in Sections 5 and 6 where they are compared with experimental results.

### 3.1. Flow stress modelling

The flow stress dependence on strain, strain rate and temperature from the compression testing is fitted to the product form Eq. 2, with the functions  $g(\bar{\varepsilon})$ ,  $h(\dot{\varepsilon})$  and  $\Theta(T)$  as in Eqs. 3 to 5. These are standard forms in the field of metal cutting (Childs and Otieno, 2012) that allow for a critical (cut-off) strain  $\bar{\varepsilon}_c$  above which strain hardening ceases (Eq. 3) and for a better fit (Eq. 4) to thermal softening than can be obtained with, for example, the single coefficient  $m$  of the Johnson-Cook equation. The product form is more convenient for fitting than an additive law such as proposed in (Zerilli and Armstrong, 1987). The coefficients of each of  $g(\bar{\varepsilon})$ ,  $h(\dot{\varepsilon})$  or  $\Theta(T)$  are obtained from varying strain, strain rate or temperature, keeping the other two constant. Previous work shows that near-identical predictions of chip formation are obtained with product and additive models provided the coefficients of the models describe similar flow stress responses in the conditions of machining (Childs and Otieno, 2012).

$$\bar{\sigma} = g(\bar{\varepsilon})h(\dot{\varepsilon})\Theta(T) \quad (2)$$

$$g(\bar{\varepsilon}) = \sigma_0 \left( 1 + \frac{\bar{\varepsilon}}{\bar{\varepsilon}_0} \right)^n, \quad \bar{\varepsilon} < \bar{\varepsilon}_c \quad (3)$$

$$g(\bar{\varepsilon}) = \sigma_0 \left( 1 + \frac{\bar{\varepsilon}_c}{\bar{\varepsilon}_0} \right)^n, \quad \bar{\varepsilon} \geq \bar{\varepsilon}_c$$

$$\Theta(T) = 1 + c_1 T + c_2 T^2, \quad 0 < T \leq T_c \quad (4)$$

$$\Theta(T) = \left( \frac{T_m - T}{T_m - T_c} \right) (1 + c_1 T_c + c_2 T_c^2), \quad T_c < T \leq T_m$$

$$h(\dot{\varepsilon}) = \left( 1 + \frac{\dot{\varepsilon}}{\dot{\varepsilon}_0} \right)^m \quad (5)$$

The coefficients of Eqs. 3 to 5 that fit the compression test results are reported in the following sub-sections. The upper and lower bounds of the coefficients from other published

works are also obtained, for subsequent use in simulation sensitivity analyses. It is convenient first to record the test results.

Fig. 4 shows the strain hardening behaviour from the plane strain compression tests. It also indicates the initial fracture strain levels from the three test repetitions, to be considered in Section 3.2.

Table 2 records the dependences of flow stress in simple compression on strain rate and temperature at a strain of 0.05. Temperature and strain rate dependence of flow stress is determined at this strain level at which heating due to plastic flow is negligible.

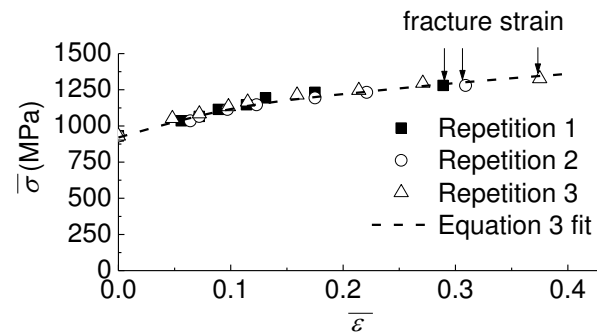


**Fig. 4.** Quasi-static strain hardening of Ti6Al4V at room temperature.

**Table 2**

Ti6Al4V flow stress (MPa) dependence on strain rate and temperature at a strain of 0.05.

Strain-rate (s <sup>-1</sup> )	Temperature (°C)			
	25	400	600	800
10 <sup>-3</sup>	1160	-	-	-
1	1230 ± 20	670 ± 20	530 ± 20	320 ± 20
10	-	730 ± 40	570 ± 50	385 ± 30
100	-	-	-	470 ± 40

### 3.1.1. Strain hardening fit to Eq. 3

The Fig. 4 results are re-plotted as flow stress relative to flow stress at zero strain in Fig. 5. Other results are added, extracted from published work on annealed or as-received (hot worked) Ti6Al4V at constant strain-rate and temperature, over the range  $20 < T(^{\circ}\text{C}) < 300$  and  $10^{-3} < \dot{\epsilon} (\text{s}^{-1}) < 10^{+3}$ . The data at high strain-rate were obtained by interrupted testing to limit heating due to plastic work. Upper and lower bounds are indicated by the dashed lines. The present work follows the lower bound.

Table 3 lists the values of  $\bar{\epsilon}_0$ ,  $n$  (Eq. 3) that fit the upper and lower bounds, and also mid-range values. Additionally, the value of  $\sigma_0$  from Fig. 4 is 930 MPa. No value is found for the cut-off strain  $\bar{\epsilon}_c$ . Fracture occurs before its level is reached. Simulations will assume either an infinite value or a value reducing with temperature, Eq.6.  $A = 20,000$ ,  $B = 0.0112$  give  $\bar{\epsilon}_c$  effectively infinite ( $\bar{\epsilon}_c > 10$ ) for  $T < 680^\circ\text{C}$  but reducing to 0.27 at  $T = 1000^\circ\text{C}$ . The latter is found to lead to improved agreements with experiment.

$$\bar{\epsilon}_c = A \exp[-BT] \quad (6)$$

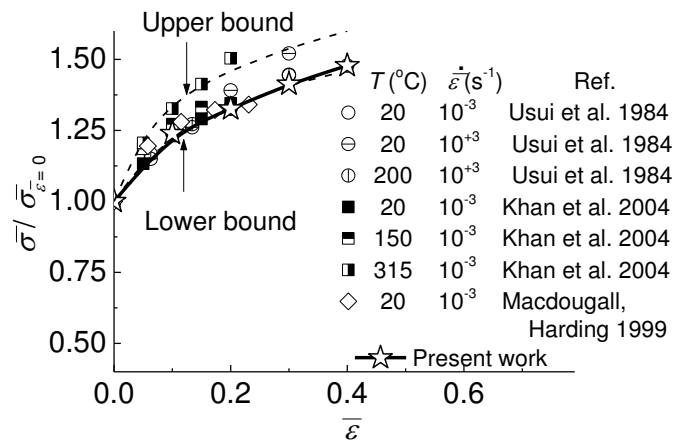


**Fig. 5.** The present strain hardening results compared to data from the literature after normalising by the flow stress at zero strain. The present work follows the lower bound.

**Table 3**

Bounding and mid values from published works of flow stress coefficients in Eqs. 3 to 5.

Bound	$\bar{\epsilon}_0$	$n$	$c_1$	$c_2$	$T_c$ ( $^\circ\text{C}$ )	$T_m$ ( $^\circ\text{C}$ )	$\dot{\bar{\epsilon}}_0$ ( $\text{s}^{-1}$ )	$m$
<b>Upper</b>	0.014	0.14	-6.1E-4	0	600	1650	0.015	0.03
<b>Mid</b>	0.022	0.145	-1.0E-3	+3.9E-7	600	1650	0.007	0.022
<b>Lower</b>	0.04	0.16	-1.4E-3	+7.8E-7	600	1650	0.001	0.015

### 3.1.2. Thermal softening fit to Eq. 4

Flow stress at  $400^\circ\text{C}$  relative to flow stress at  $25^\circ\text{C}$  is obtained from Table 2 at a strain rate of 1/s. Flow stress at temperatures of 600 and  $800^\circ\text{C}$  relative to flow stress at  $400^\circ\text{C}$  is obtained in two ways, at strain rates of 1 and 10/s, and averaged. The relative

thermal softening over the complete range 25 to 800°C is obtained stepwise. The results and their comparison with data extracted from published work are in Fig. 6

The data shown as solid symbols in Fig. 6 are from tests either at  $T < 450^\circ\text{C}$  or at strain rates  $> 10^3/\text{s}$ . The dashed lines are bounds to these. Their Eq. 4 coefficients are in Table 3. The present results follow the lower bound for  $T < 600^\circ\text{C}$  but at  $T = 800^\circ\text{C}$  (circled) they fall below the lower bound, as do results from previous work at the strain rates of  $10^{-3}$  and  $1/\text{s}$  (El-Magd et al., 2006). These high temperature, low strain rate, conditions do not occur during chip formation at engineering speeds and feeds and are regarded as not relevant.

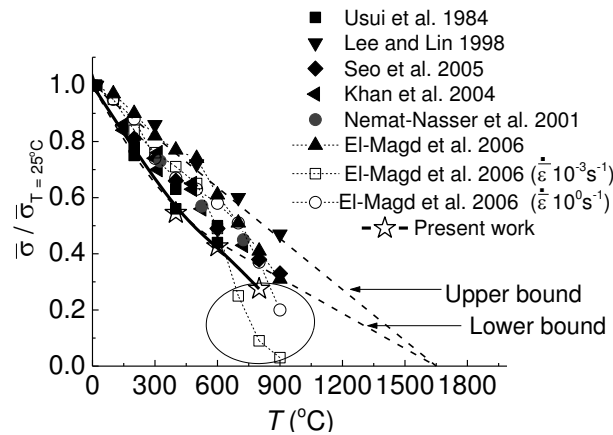


**Fig. 6.** Flow stress at temperature relative to flow stress at 25°C from the present and previous works. The present work follows the lower bound in machining-relevant conditions.

### 3.1.3. Strain rate hardening fit to Eq. 5

Flow stress results at high strain rate relative to flow stress at  $\dot{\epsilon} = 10^{-3}/\text{s}$  from the present and published works are in Fig. 7. The present results are obtained from Table 2 in a stepwise fashion, hardening from  $\dot{\epsilon} = 10^{-3}$  to  $1.0/\text{s}$  being obtained at  $T = 25^\circ\text{C}$ , from 1 to  $10/\text{s}$  at 400, 600 and  $800^\circ\text{C}$  and from 10 to  $100/\text{s}$  at  $800^\circ\text{C}$ . The previous work data are from room temperature testing except for that from (El-Magd, 2006) which is averaged over the range 20 to  $600^\circ\text{C}$ . The upper and lower bounds to the previous work are marked, with their Eq. 5 coefficients in Table 3. The present result for  $\dot{\epsilon} = 100/\text{s}$ , dependent on the  $800^\circ\text{C}$  data, is above

the upper bound from the previous work. It is regarded as an overestimate for machining-relevant conditions, in the same way as is the thermal softening at 800°C in Fig. 6.

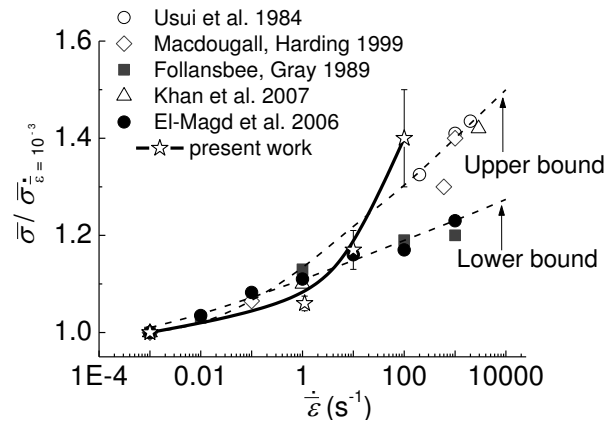


**Fig. 7.** Flow stress at  $\dot{\epsilon} > 10^{-3}$  /s relative to flow stress at  $\dot{\epsilon} = 10^{-3}$  /s from the present and previous works.

### 3.2. Failure modelling

It is observed that in the low speed machining of Ti6Al4V (Fig. 1, billet A) the chip segments are not separated. Presumably, under compression, traction occurs across the interfaces between segments as the segments develop. A discontinuity in micro-structure across the interfaces is also observed. The interfacial condition is called shear failure here even though failure more commonly is used to describe the fragmentation and complete loss of traction that occurs in tensile conditions. Further, the interfaces are not regarded as external boundaries to the segments to either side of them. The model assumes that the segments and their interfaces are a continuum. A reduced flow stress develops in the interfacial region. In this way a unified view is developed from low speed to high speed machining. At low speed failure governs the complete cycle of segment development. At high speed it provides another way, in addition to thermal softening, to trigger shear banding. The development of the banding then becomes also dependent on adiabatic shear.

Failure is considered in two stages: its initiation followed by the flow stress reduction in the interfacial region that it causes.

### 3.2.1. Failure initiation

Mainstream current advances in modelling ductile shear failure, mainly applied in conditions of positive stress triaxiality,  $\eta$ , assume a Mohr- Coulomb failure law. (Bai and Wierzbicki, 2010) show that in plane strain conditions the Mohr-Coulomb law leads to an approximately exponential dependence of failure strain on  $\eta$ . The exponential form is assumed here, extrapolated into negative  $\eta$  conditions, with increase of damage  $D$  along a streamline, and the onset of failure as  $D$  reaches 1.0, as in Eq. 1.

Published data for shear failure of Ti6Al4V at room temperature and low strain rate reviewed in the Introduction give a range for  $\varepsilon_{f,0}$  of  $\approx 0.25$  to  $0.5$  and for  $c \approx -0.5$  to  $-2.0$ . Further data exist for elevated temperatures and strain rates. The commonly quoted work (Johnson and Holmquist, 1989) and all other studies, from Usui et al. (1984), through Macdougall and Harding (1999) to Hammer (2012) show a negligible influence of strain rate on failure strain. However there is a significant influence of temperature that can be approximated to a linear increase of  $\varepsilon_{f,0}$  with  $T$  up to some critical value  $T_{crit}$  above which it increases rapidly. Eq. 7 will be assumed here. Estimates for  $a$ , from predominantly tensile testing, are  $0.0023$  (Johnson and Holmquist, 1989) and  $0.0012$  (Hammer, 2012), with testing at  $T$  up to  $450^\circ\text{C}$  and  $600^\circ\text{C}$  respectively and no indication of a value for  $T_{crit}$ . Data from compression testing up to  $400^\circ\text{C}$  (Kailas et al., 1994) gives  $a = 0.0022$ , with the comment that at  $400^\circ\text{C}$  failure is no longer catastrophic as it is at lower temperature. Data in (El-Magd et al., 2005) show a major increase in failure strain between  $600$  and  $700^\circ\text{C}$ . Here  $T_{crit} = 600^\circ\text{C}$  is assumed. The effect of varying  $a$  in the range  $0$  to  $0.0024$  is treated in Section 6.

Values for  $\varepsilon_{f,0}$  and  $c$  are chosen to give agreement between predicted and observed chip formation at low cutting speed, taking account of their expected ranges and the fracture strains in plane strain compression (Fig. 4).

$$\begin{aligned} (\varepsilon_{f0})_{T^{\circ}\text{C}} &= \varepsilon_{f0}(1 + aT), & T < T_{\text{crit}} \\ (\varepsilon_{f0})_{T^{\circ}\text{C}} &= \infty, & T > T_{\text{crit}} \end{aligned} \quad (7)$$

### 3.2.2. The failed flow stress behaviour

It is pictured physically that under low compressive hydrostatic pressure  $p$  the shear flow stress  $\tau_D$  of failed material is in proportion to  $p$  according to  $\tau_D = \mu_i p$ , with  $\mu_i$  having the character of an internal Coulomb friction coefficient. Then the failed flow stress  $\bar{\sigma}_D$  is  $\tau_D \sqrt{3}$ .

At high pressure  $\bar{\sigma}_D$  becomes limited to  $\bar{\sigma}$ , the flow stress of the undamaged material.

Considering that  $p/\bar{\sigma}$  is equivalent to  $-\eta$ , then the ratio of failed to undamaged flow stress  $\bar{\sigma}_D/\bar{\sigma}$  may be written as varying from  $(-\sqrt{3}\mu_i\eta)$  to 1.0 as  $\eta$  becomes increasingly negative.

It is further pictured that a failed material heals if its temperature during subsequent deformation rises to a sufficient level, i.e. flow stress can return to  $\bar{\sigma}$  and  $D$  to zero. It is supposed that healing occurs between lower and upper temperature limits,  $T_L$  and  $T_U$ , with the extent of healing varying linearly from 0 to 100% between those limits

Eqs. 8 describe the proposed behaviour.  $f(\eta, T)$  is the ratio of  $\bar{\sigma}_D$  to  $\bar{\sigma}$ . A tanh function is taken empirically to represent its dependence on  $\eta$  for  $T < T_L$ . Fig. 8's solid line illustrates this for the example  $\mu_i = 1.0$ . The chained line shows the fully healed condition when  $T > T_U$ . The dashed line is an intermediate state, in fact when  $T$  is halfway between  $T_L$  and  $T_U$ . A zero value of  $\bar{\sigma}_D$  is prevented by a minimum allowed value of  $f(\eta, T)$ .

Values are chosen  $T_L = 600^\circ\text{C}$ , to match  $T_{\text{crit}}$  (Eq. 7);  $T_U = 700^\circ\text{C}$ ;  $f(\eta, T)_{\text{min}} = 0.1$ .  $\mu_i$  is adjusted, with  $\varepsilon_{f,0}$  and  $c$ , to give agreement between predicted and observed low speed chip formation ( $\mu_i \approx 1.0$  is determined)

$$\begin{aligned}
\bar{\sigma}_D &= f(\eta, T) \bar{\sigma} \\
f(\eta, T) &= \tanh[-\sqrt{3}\mu_i\eta] & T < T_L \\
&= 1.0 & T > T_U \\
&= \tanh[-\mu_i\eta] + (1 - \tanh[-\sqrt{3}\mu_i\eta]) \left( \frac{T - T_L}{T_U - T_L} \right), & T_L < T < T_U \\
&\text{subject to } f(\eta, T) > f(\eta, T)_{\min}
\end{aligned} \tag{8}$$

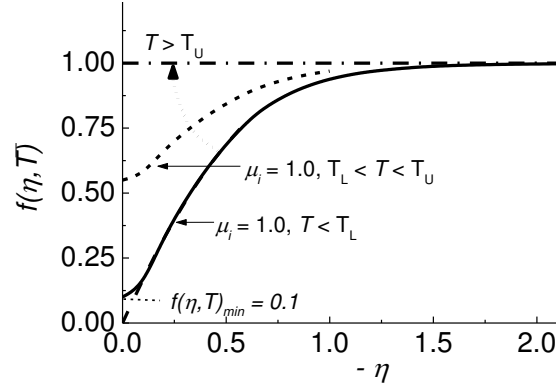


**Fig. 8.** Example dependence of the ratio of failed to undamaged flow stress on  $\eta$  and  $T$ .

### 3.3. Work and tool thermo-physical properties and the chip / tool friction model.

The thermal conductivity and heat capacity of Ti6Al4V are taken to be independent of temperature and equal to 6.7 W/m°C and 2.3 MJ/m<sup>3</sup>. The H13A tool thermal conductivity is taken to be 100 W/m°C (Mondelin et al., 2013). Its heat capacity  $\rho C$  is taken to be 0.1 MJ/m<sup>3</sup>. This is a 36-fold reduction from its physical value and reduces the time taken to reach the steady state temperature without changing the steady state value (Arrazola et al., 2015). Fig. 9 demonstrates this for the example  $v_c = 80$  m/min,  $h = 0.25$  mm. When  $\rho C = 0.1$  MJ/m<sup>3</sup> the maximum rake face temperature reaches a steady value after  $\approx 0.5$  ms. After  $\approx 1$  ms the tool temperature contours show heat to be diffused well below the chip / tool contact. When  $\rho C = 3.6$  MJ/m<sup>3</sup> the steady state maximum rake temperature is still not quite achieved after 2.3 ms and the tool subsurface temperatures are far from steady state.

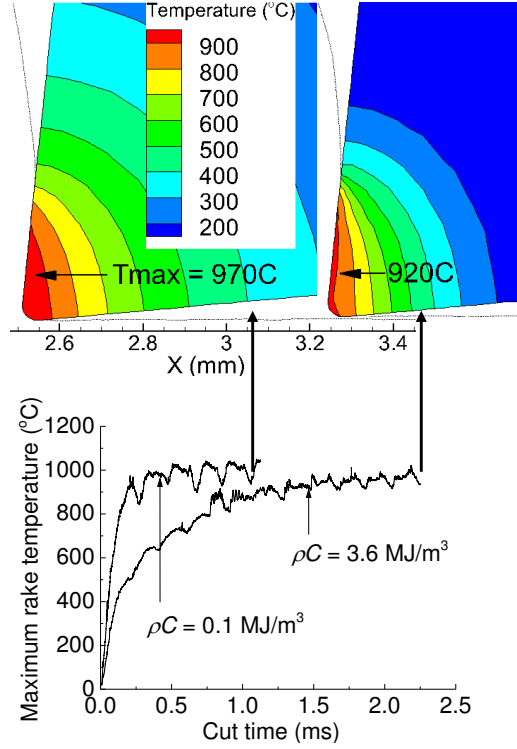


**Fig. 9.** Simulated influence of tool heat capacity  $\rho C$  on tool temperature development with time in machining Ti6Al4V, example of  $v_c = 80$  m/min,  $h = 0.25$  mm. Maximum rake temperature is shown below with (above) tool temperature distributions after  $\approx 1$  ms ( $\rho C = 0.1$  MJ/m<sup>3</sup>) and 2.3 ms ( $\rho C = 3.6$  MJ/m<sup>3</sup>).

The chip / tool sliding friction law is given by Eq. 9 ( $\tau_f$  is friction stress,  $\sigma_n$  is normal stress,  $\mu$  is the friction coefficient; when  $D = 1$   $\bar{\sigma}$  is replaced by  $\bar{\sigma}_D$ ).  $\mu$  is set to 1.0. Then  $\tau_f$  depends on  $\bar{\sigma}$  (or  $\bar{\sigma}_D$ ) over most of the contact (Childs, 2013). The failure model affects both the flow stress in the primary shear region and the friction stress between chip and tool.

It should be noted that  $\mu$  is an input to the simulations. It differs from  $\tan^{-1}\lambda$ , with  $\lambda$  the friction angle between the resultant cutting force and the normal to the tool rake face, because  $\tau$  is not equal to  $\sigma_n$  over the whole of the chip / tool contact.

$$\tau = \min(\mu\sigma_n, \bar{\sigma}/\sqrt{3}) \quad (9)$$

### 3.4. Simulation conditions.

The material flow stress and damage models are implemented as user-defined sub-routines in the commercial machining simulation software AdvantEdge™-2D v. 7.3.

Simulations have been carried out over the experimental range of  $h$  and  $v_c$ , with tool rake angle  $6^\circ$  and clearance angle  $5^\circ$  and cutting edge radii  $r_\beta$   $10\ \mu\text{m}$  and  $35\ \mu\text{m}$  (to match the tools used in the low and high speed cutting tests).

In all cases except two, the Ti6Al4V flow stress is as measured ( $\sigma_0 = 930\ \text{MPa}$  and Table 3 lower bound coefficients for strain hardening and thermal softening and upper bound coefficients for strain rate hardening), with the addition of two options for cut-off strain  $\bar{\varepsilon}_c$  : in Eq. 6,  $A = 20,000$  and  $B =$  either zero or  $0.0112$ . The case  $B =$  zero effectively gives an infinite cut-off strain.

The first of the two exceptions is to suppose a pre-strain of  $0.1$  in the strain hardening behaviour. Its purpose is to simulate in an approximate way the influence of changed flow stress in the cut surface caused by a previous pass of the tool. It is achieved by changing the coefficients of Eq. 3 to  $\sigma_0 = 1140\ \text{MPa}$ , and  $\bar{\varepsilon}_0 = 0.14$ , leaving  $n$  unchanged. The second supports a general sensitivity study, replacing all the flow stress coefficients by their mid-values (Table 3).

Damage and failure parameters  $\varepsilon_{f,0}$ ,  $c$  (Eq. 1),  $a$  (Eq. 7) and  $\mu_i$  (Eq. 8) have been varied. Their influences are reported in Section 4. Values finally selected, validated mainly in Sections 5 but also (for  $a$ ) in Section 6, are  $(\varepsilon_{f,0}, c) = (0.25, -1.5)$  and  $(0.3, -1.0)$ ,  $a = 0.0012$  and  $\mu_i = 1.0$ . Simulations have also been carried out omitting the failure model.

The simulations in Sections 4 to 6 consider a single pass of the tool over a virgin surface (or, in the case of pre-strain, a uniformly pre-strained surface). They have been carried out with the software in its standard mode of use (see next paragraph). The software

has a second, special mode (also next paragraph) that allows a second pass to be simulated, over a surface that accurately contains strain and damage profiles from the previous pass. Results from two simulations from this mode of use are included in the discussion Section 7. They give grounds for the introduction of the pre-strain approximation.

AdvantEdge™, developed from (Marusich and Ortiz, 1995), is a coupled thermo-elasto-plastic Lagrangian code with continuous re-meshing and adaptive meshing that can be controlled by the user. In its standard use the mesh automatically coarsens away from the cutting zone. This reduces the elapsed computing time but loses resolution of field variables. In a special use the coarsening can be prevented in the cut surface, but at the expense of increasing the computing time. In the present case a minimum mesh size of 2  $\mu\text{m}$  is required to resolve chip serration. Elapsed simulation time depends on  $h$  and  $v_c$ . In standard use the elapsed time per mm cut distance ranges from  $\approx 5$  hrs for  $h = 0.1$  mm,  $v_c = 80$  m/min to  $\approx 4$  days for  $h = 0.25$  mm and  $v_c = 1$  m/min, with an 8-core parallel 3.6 GHz CPU. In the special use elapsed times are at least ten times longer.

It is not possible with this software to delete elements in failed regions, thereby opening up new (cracked) surfaces. It is only possible to identify failed ( $D = 1$ ) regions and determine the predicted flow stresses within them, with low stress values identifying where failure (a crack) would occur. This limitation is taken to be unimportant in the present application in which shear cracks under compression do not significantly open up (Fig. 1).

#### **4. Simulated chip formation: general observations**

The general characteristics of chip formation with the failure model are outlined here, compared to chip formation without the failure model. In all cases  $\mu = 1$  (Eq. 9) is applied.

Without the failure model, large changes in chip formation occur with increasing  $h v_c$ , as illustrated in Fig. 10 (for the example of infinite  $\bar{\varepsilon}_c$  and  $r_\beta = 10 \mu\text{m}$ ). At the lowest  $h, v_c$  (Fig. 10a,  $h = 0.1 \text{ mm}, v_c = 1 \text{ m/min}$ ) a high friction stress, unmitigated by thermal softening, exists at the chip / tool contact such that steady chip formation is not reached even after a cut distance  $10h$ . Increasing  $h$  to  $0.2 \text{ mm}$  and  $v_c$  to  $30 \text{ m/min}$  (Fig. 10b) causes thermal softening at the chip / tool contact and a reduced friction stress: a steady chip is created in a cut distance  $\ll 5h$ . A small further increase in  $v_c$  to  $40 \text{ m/min}$  (Fig. 10c) initiates a small cyclic variation in the chip thickness. Further increasing  $h$  to  $0.25 \text{ mm}$  and  $v_c$  to  $80 \text{ m/min}$  (Fig. 10d) results in more severe cyclic variation but the serrations do not match experimental observations (Fig. 1).

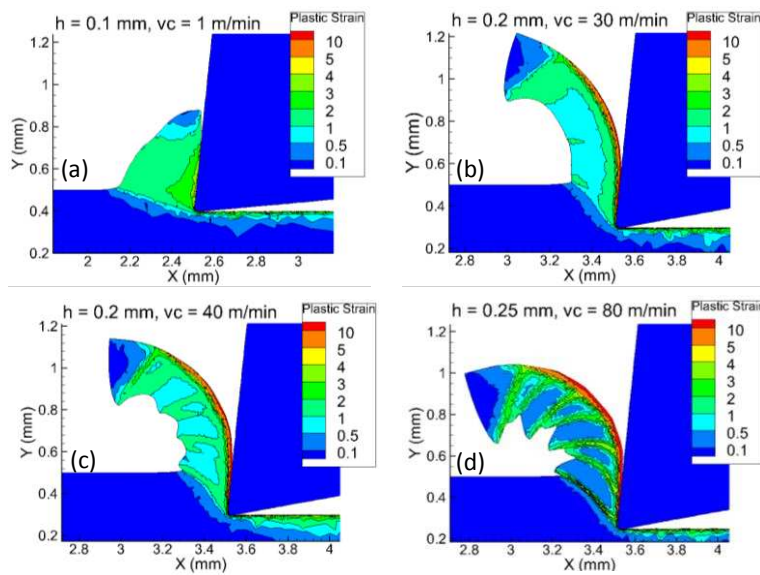


**Fig. 10.** Simulated chip formations with no damage model and  $\mu = 1$ , cut distance  $1 \text{ mm}$ ,  $h v_c$  ( $\text{mm}^2/\text{s}$ ) = (a) 1.7, (b) 100, (c) 130, (d) 330.

The boundary between steady and cyclic chip formation without the failure model is found to occur at  $h v_c = 125 \text{ mm}^2/\text{s}$ , as shown in Fig. 11a. It corresponds to the onset of adiabatic conditions from previous work (Table 1). Including the damage model causes serrated chip formation for  $h v_c < 125 \text{ mm}^2/\text{s}$  and changes the serration quality for  $h v_c > 125 \text{ mm}^2/\text{s}$ . Figs. 11b to d show three examples (for  $\varepsilon_{f,0} = 0.25$ ,  $c = -1.5$ ,  $a = 0.0024$ ,  $\mu_i = 1.0$ ).

Figs. 11b and c are for the same  $h$ ,  $v_c$  as Figs.10d and a. Fig. 11d is a further example of  $h v_c < 125 \text{ mm}^2/\text{s}$ : its combination  $h = 0.1 \text{ mm}$ ,  $v_c = 40 \text{ m/min}$  is at the lower limit of the high speed cutting tests (Section 6).

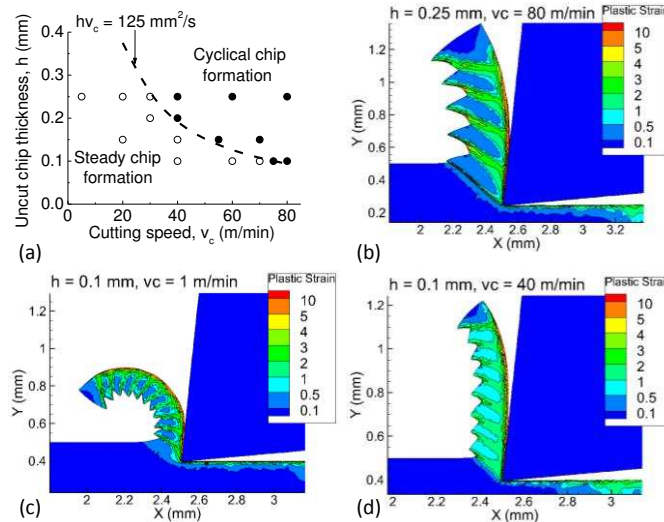


**Fig. 11.** (a) the boundary between steady and cyclic chip formation with no damage model; b to d examples of chip formation with a damage model ( $h$ ,  $v_c$  as marked, cut distance 1 mm).

Figs. 12 and 13 give more detail of the conditions of chip formation for the same examples as in Fig. 11. Fig. 12 shows contours of damage  $D$  and flow stress at instants just after the start of localised shear. For  $h = 0.1 \text{ mm}$ ,  $v_c = 1 \text{ m/min}$  (Fig. 12 column a), material has failed ( $D = 1$ ) over the entire length of the primary shear zone and in the secondary shear zone too. Flow stress in the primary zone is reduced by failure to 240 MPa near the free surface and is also reduced towards the rear of the chip / tool contact: the flow stress gradient along the contact is consistent with the curled chip of Fig. 11c.

For  $h = 0.1 \text{ mm}$ ,  $v_c = 40 \text{ m/min}$  (Fig. 12 column b),  $D = 1$  over only  $\approx$  half the length of the primary zone. Damage is healed in the secondary zone. The flow stress in the primary zone near the free surface is 200 MPa but healing has increased it to a uniformly high value of 1300 MPa along the chip / tool contact (consistent with the straighter chip in Fig. 11d).

For  $h = 0.25 \text{ mm}$ ,  $v_c = 80 \text{ m/min}$  (Fig. 12 column c),  $D = 1$  over the majority of the primary zone. Healing has occurred in the secondary zone and also in the previously created

primary zone. The flow stress in the primary zone near the free surface is 300 MPa; in the secondary zone it is reduced by thermal softening to 980 MPa compared to its value of 1300 MPa when  $h = 0.1$  mm,  $v_c = 40$  m/min.

In all three cases, flow stress is low (200 to 300 MPa) at the free surface in the serration roots, indicating cracking to be likely there.

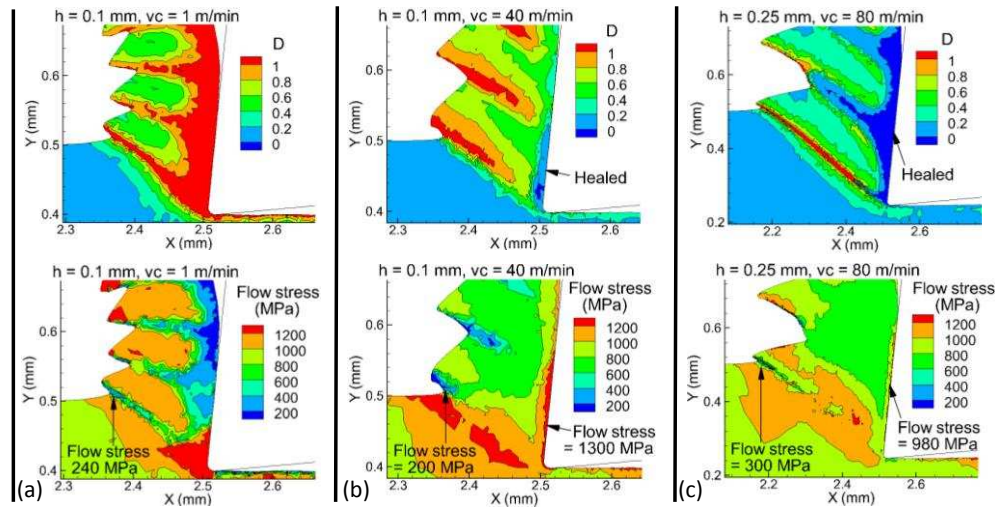


**Fig. 12.** Contours of  $D$  and flow stress at the start of localised shear: column (a)  $h = 0.1$  mm,  $v_c = 1$  m/min, column (b)  $h = 0.1$  mm,  $v_c = 40$  m/min, column (c)  $h = 0.25$  mm,  $v_c = 80$  m/min.

Fig. 13 gives further insight into these observations. It shows contours of  $D$ ,  $\eta$ , temperature and strain just before the start of the localised shears in Fig. 12. Although in all three cases of Fig. 12, failure causes the shear stress in the primary zone to be low at the free surface, Fig. 13a shows failure to be initiated ( $D = 1$ ) at different positions in the shear zone. It is initiated at the cutting edge for  $h = 0.1$  mm,  $v_c = 1$  m/min, at the free surface for  $h = 0.1$  mm,  $v_c = 40$  m/min, while for  $h = 0.25$  mm,  $v_c = 80$  m/min failure is more uniformly distributed along the mid-half of the shear zone.

The changed initiation site between  $h = 0.1$  mm,  $v_c = 1$  m/min and  $h = 0.1$  mm,  $v_c = 40$  m/min is caused by the changed stress triaxiality (Fig. 13b). Increasingly negative triaxiality at the cutting edge suppresses failure there. It is a consequence of thermal softening in the primary zone, the reverse of the influence of strain hardening (Oxley, 1989). The

further change as  $h$  increases to 0.25 mm and  $v_c$  to 80 m/min is also due to thermal softening but in the secondary zone. It reduces the chip / tool friction stress (Fig. 12c) which in turn changes chip flow by allowing easier sliding of the chip over the tool. The temperature in both the primary and secondary shear zones are shown in Fig. 13c: in the primary zone increasing from 150°C, through 400°C, to 500°C with increasing  $h v_c$ ; on the rake face from  $\approx 70^\circ\text{C}$ , to  $\approx 700^\circ\text{C}$ , to almost 1000°C.

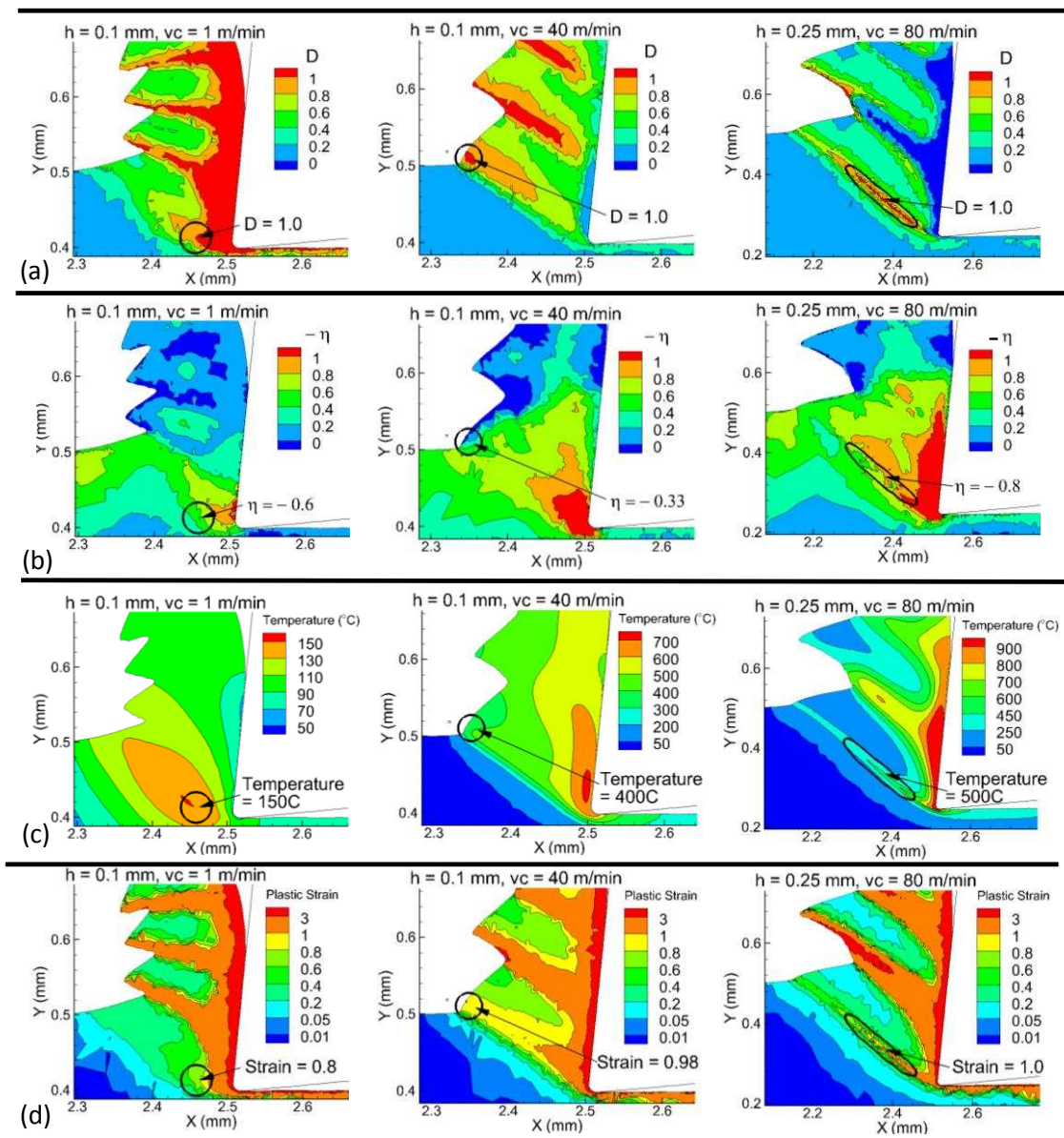


**Fig. 13.** Contours of (a)  $D$ , (b)  $\eta$ , (c) temperature and (d) plastic strain, just before the start of localised shear, columns left to right as Fig. 12.

In all three cases, the strain at the start of failure (Fig. 13d) is  $\approx 1.0$  (0.8 at  $h = 0.1$  mm,  $v_c = 1$  m/min). At the lowest and highest  $h v_c$ , stress triaxiality along the strain path (Fig.

13b) has fallen (more compressive) to the range - 0.6 to - 0.8. In the intermediate  $hv_c$  case, triaxiality has passed through that range and at the instant of Fig. 13 it has risen to - 0.33. Temperature  $< 500^\circ\text{C}$  in all cases. These are the relevant conditions for the failure model.

The predictions of Figs. 12 and 13 agree with and help to resolve differences between historical studies of cracking in Ti6Al4V chip formation. (Komanduri and von Turkovich, 1981) report crack initiation at the cutting edge at  $v_c \approx 1$  mm/min,  $h \approx 0.1$  mm, converting to failure at the free surface as serration progresses. This is as predicted in columns (a) of Figs. 12 and 13. Vyas and Shaw (1999) show cracking predominantly at the free surface as well as micro-cracks within the central region of the shear band serration, for  $v_c \approx 50$  m/min,  $h \approx 0.2$  mm. This is the case of columns (c).

Figs. 12 and 13 are for the case  $\varepsilon_{f,0} = 0.25$ ,  $c = - 1.5$ ,  $a = 0.0024$  and  $\mu_i = 1.0$ . Changing these changes the cutting and thrust forces and chip serration amplitude. Fig. 14 shows effects of varying  $c$  and  $\mu_i$  in a low speed case ( $h = 0.1$  mm,  $v_c = 10$  m/min), with  $\varepsilon_{f,0} = 0.25$  and  $a = 0.0024$  kept constant. An increasingly negative  $c$  increases all of  $F_C^*$ ,  $t_{\max}/h$  and  $t_{\min}/h$  but the ratio of  $t_{\max}/h$  to  $t_{\min}/h$  reduces. When  $c = - 2.5$ ,  $t_{\max}/h = t_{\min}/h$ , i.e. the chip is not segmented. Increasing  $\mu_i$  mainly increases  $t_{\min}/h$  relative to  $t_{\max}/h$ , i.e. the segmentation becomes less severe. These effects of  $c$  and  $\mu_i$  are qualitatively as expected. A more negative  $c$  increases failure strain, leading to an overall thicker chip. Increasing  $\mu_i$  leads to a lower reduction of flow stress of failed material, in turn causing more resistance to serration. Increasing  $\varepsilon_{f,0}$  has a similar effect to negatively increasing  $c$ .

The failure model coefficients also influence the chip serration pitch. Fig. 15 illustrates this for two conditions from Fig. 14:  $\varepsilon_{f,0} = 0.25$  and  $\mu_i = 1.0$ , and  $c = - 0.5$  and  $- 1.9$ . The more negative  $c$  gives a larger pitch. At high cutting speed  $a$  also affects pitch. In the example of Fig. 16, for  $h = 0.25$  mm,  $v_c = 80$  m/min, pitch increases as  $a$  increases from  $a = 0$  (Fig. 16a) to  $a = 0.0024$  (Fig. 16b).

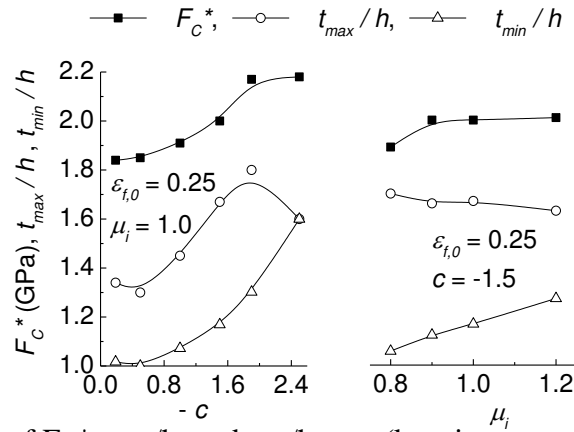


**Fig. 14.** Dependence of  $F_C^*$ ,  $t_{max}/h$ , and  $t_{min}/h$  on  $c$  (keeping  $\epsilon_{f,0}$  and  $\mu_i$  constant) and  $\mu_i$  (keeping  $\epsilon_{f,0}$  and  $c$  constant) for the example  $h = 0.1$  mm,  $v_c = 10$  m/min.

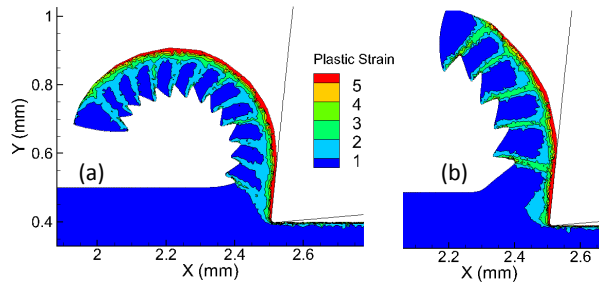


**Fig. 15.** Chip serration pitch shown after a cut distance 1 mm, for  $c =$  (a) -0.5, (b) -1.9, other conditions as Fig. 14.

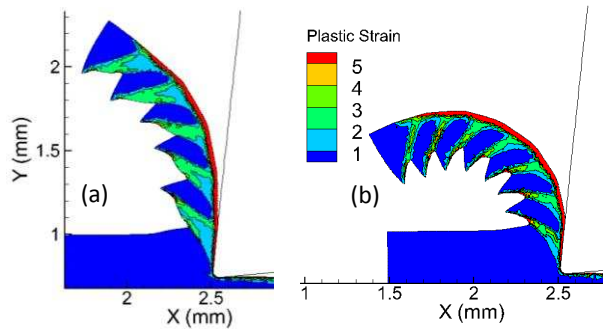


**Fig. 16.** Chip serration pitch for  $h = 0.25$  mm,  $v_c = 80$  m/min shown after a cut distance 1.5 mm, for  $a =$  (a) 0, (b) 0.0024, other conditions  $\epsilon_{f,0} = 0.25$ ,  $c = -1.5$ ,  $\mu_i = 1.0$ , also (Eq. 6)  $A = 20,000$ ,  $B = 0.0112$ .

## 5. Low cutting speed experimental and simulation results

Experimentally measured cutting forces at low cutting speed oscillate with cut distance. A portion of the recorded cutting and thrust force signal is shown for two examples

in Fig. 17a. Forces are converted to specific forces and cut distance is expressed as multiples of  $h$ . The cutting force oscillation in particular is larger for the lower  $v_c$ , larger  $h$ , condition ( $v_c = 1$  m/min,  $h = 0.25$  mm). Oscillation amplitude, expressed as  $F_{C^*_{max}}/F_{C^*_{min}}$ , is found (Fig. 17b), for a wider range of  $h$  and  $v_c$ , to reduce with increasing frequency  $v_c/h$ . It becomes minor for  $v_c/h > 200$  to 300 Hz (Fig. 17a's  $v_c = 3$  m/min,  $h = 0.1$  mm is an example). Video frames show the force oscillations for  $v_c/h < 300$  Hz to be synchronised with tool deflection oscillations in the cutting direction. Tool oscillation is not seen above 300 Hz. This overall behaviour is consistent with chip segmentation driven tool oscillation below the measured tool holder and support resonant frequency of 160 Hz and with damping above it.

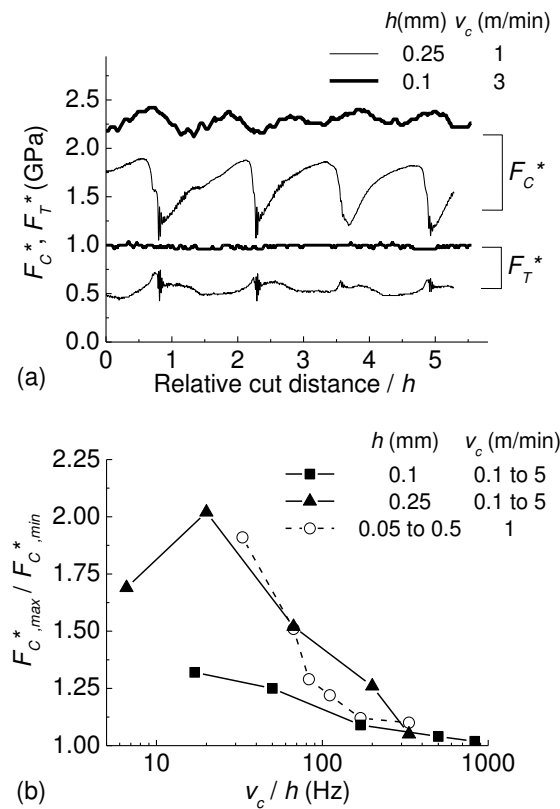


**Fig. 17.** (a) example oscillations of measured specific forces  $F_C^*$  and  $F_T^*$  with cut distance and (b) dependence of maximum to minimum cutting force ratio on  $v_c/h$ :  $h$  and  $v_c$  as marked.

The observed low frequency tool deflections have peak to trough size up to  $0.4h$  (for  $F_{C^*_{max}}/F_{C^*_{min}} \approx 2$  in Fig. 17b). The modelling and simulations assume a fixed tool. It is the condition  $v_c/h > 200$  Hz that is suitable for validating the failure model. On the other hand  $h v_c$

$< 70 \text{ mm}^2/\text{s}$  is necessary to avoid adiabatic conditions (Table 1). These give a range of  $v_c$  for validation from 1 to 40 m/min for  $h = 0.1 \text{ mm}$  and 3 to 15 m/min for  $h = 0.25 \text{ mm}$ .

Experimental and simulated specific forces from  $v_c = 1$  to 30 m/min are compared in Fig. 18a. Forces are R.M.S. averages from outputs as in Fig. 17a and from the equivalent simulated observations.  $t_{\max}/h$  and  $t_{\min}/h$  are compared in Figs. 18 b and c. The simulations are with  $r_\beta = 10 \text{ }\mu\text{m}$  and the flow stress model with infinite cut off strain. The failure coefficients are  $\varepsilon_{f,0} = 0.25$ ,  $c = -1.5$ ,  $\mu_i = 1.0$ . The simulations give agreement with experiments for both forces and chip dimensions except at  $h = 0.25 \text{ mm}$ ,  $v_c = 30 \text{ m/min}$ . Then the experimental  $t_{\max}/h$  and  $t_{\min}/h$  fall below the simulated values. This condition is outside the validation range. Other simulations (not shown) with  $\varepsilon_{f,0} = 0.3$ ,  $c = -1.0$  are insignificantly different from those with  $\varepsilon_{f,0} = 0.25$ ,  $c = -1.5$  as far as the variables of Fig. 18 are concerned.

The simulations are less successful at predicting the chip segmentation pitch. Fig. 19 compares experimental and simulated chip sections for  $h = 0.1 \text{ mm}$  and  $v_c = 10 \text{ m/min}$ . Experimental results from two collected chips are shown. They show a typical variability between samples. The simulations are for both  $\varepsilon_{f,0} = 0.25$ ,  $c = -1.5$  and  $\varepsilon_{f,0} = 0.3$ ,  $c = -1.0$ . In the latter case, the pitch is less than in the former case, though both cases show a larger than experimental pitch (this is considered further in Section 7).

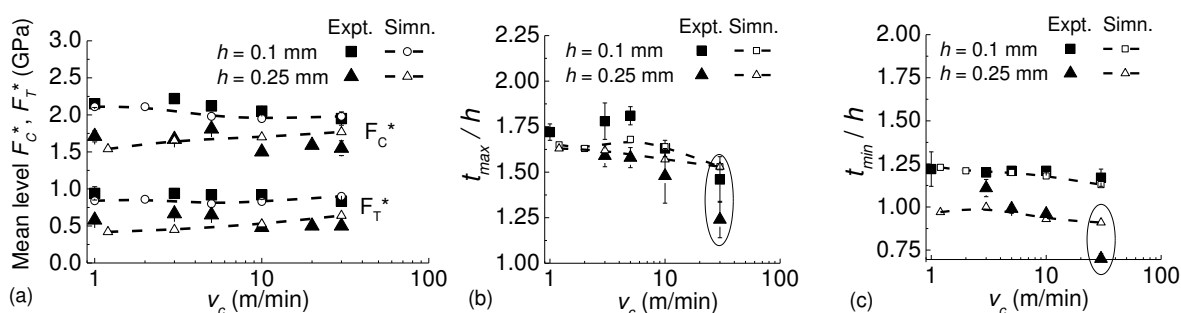


**Fig. 18.** Experimental and simulated dependences on  $v_c$ , for  $h = 0.1$  and  $0.25 \text{ mm}$ , of (a)  $F_C^*$ ,  $F_T^*$ , (b)  $t_{\max}/h$ , and (c)  $t_{\min}/h$ . The experimental and simulated  $t_{\max}/h$  and  $t_{\min}/h$  (circled) diverge at  $h = 0.25 \text{ mm}$ ,  $v_c = 30 \text{ m/min}$ .

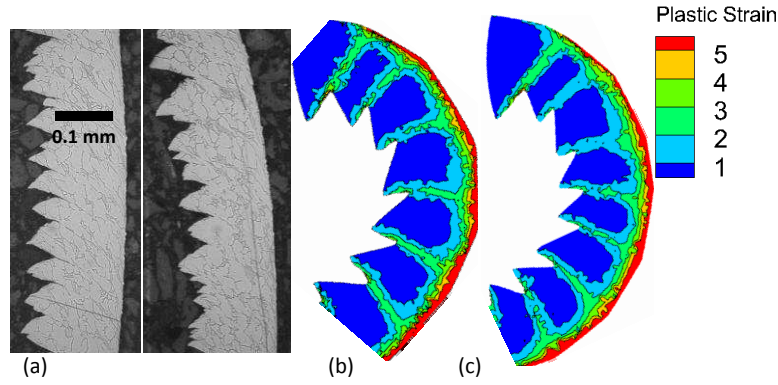


**Fig. 19.** Comparisons of chip sections,  $h = 0.1$  mm,  $v_c = 10$  m/min, all to the same scale: (a) experiments, (b, c) simulations with  $(\epsilon_{f,0}, c) =$  (b) 0.25, - 1.5, (c) 0.3, - 1.0.

## 6. Higher cutting speed experimental and simulation results

Fig. 16 demonstrates the influence of  $a$  on chip pitch, for  $a = 0$  and  $a = 0.0024$ , for  $h = 0.25$  mm,  $v_c = 80$  m/min. Fig. 20 compares experimental and simulated chip shapes for the intermediate value  $a = 0.0012$ . On this basis  $a = 0.0012$  is selected for further simulations.

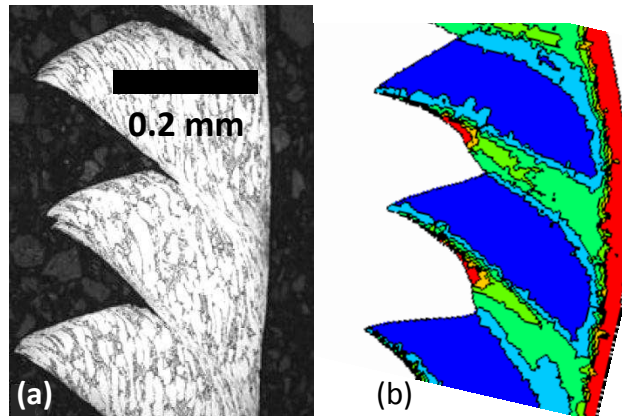


**Fig. 20.** Comparison of chip sections,  $h = 0.25$  mm,  $v_c = 80$  m/min, both to the same scale: (a) experiment, (b) simulation, with conditions as Fig. 16 except  $a = 0.0012$ . Simulation contours are strain from 1 to 5 in 5 equal steps.

Experimental and simulated values of  $t_{max}/h$  and  $t_{min}/h$  from the high speed tests are compared in Figs. 21a, b. The abscissa is taken as  $h v_c$ . A wide scatter in the experimental results is due at least in part to real variations and limited data collected from chip sections, as

also found in the low speed observations (Fig. 19).  $t_{\max}/h$  remains in the range  $\approx 1.2$  to  $1.4$  for all  $h v_c$ .  $t_{\min}/h$  reduces from  $\approx 1.05$  to  $0.75$  as  $h v_c$  increases to  $\approx 150 \text{ mm}^2/\text{s}$  and remains in the range  $\approx 0.7$  to  $0.8$  thereafter. Three sets of simulations are included, all with  $r_\beta = 35 \text{ }\mu\text{m}$  and  $\varepsilon_{f,0}$ ,  $c$ ,  $\mu_i$  from Section 5. They are for two values of  $h$ ,  $0.1$  and  $0.25 \text{ mm}$ . The first set ( $A = 20000$ ,  $B = 0$ ) assumes an infinite cut-off strain. Simulations with  $h = 0.1$  and  $0.25 \text{ mm}$  fall on the same trajectory and overestimate the experimental values. Introducing a cut-off strain reducing with temperature ( $B = 0.0112$ ) separates the  $h = 0.1$  and  $0.25 \text{ mm}$  simulations and moves them towards the experimental results. A further modification is needed to move the simulations into the experimental ranges. The third set of simulations in Fig. 21 achieves this. It supposes a pre-strain of  $0.1$  to exist in the work (see Section 3.4). It is imagined that this is a proxy for the effect of the real damage and strain distribution in the cut surface from the previous pass of the tool, as considered further in Section 7.

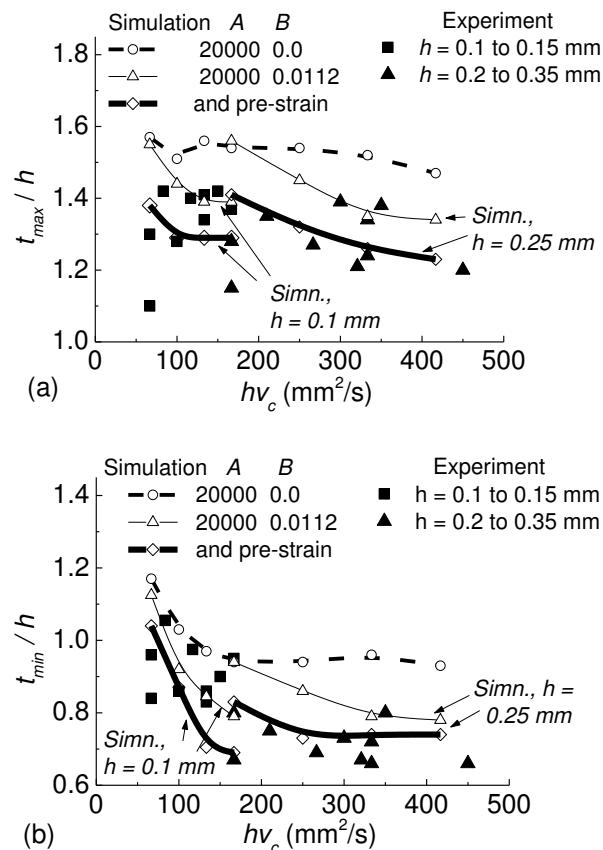


**Fig. 21.** Comparisons of experimental and simulated dependencies on  $h v_c$  of (a)  $t_{\max}/h$  and (b)  $t_{\min}/h$ , in higher speed cutting conditions.

Predicted specific forces and maximum tool temperature rises  $\Delta T$  from all three sets of simulations are compared to experimental results in Figs. 22 and 23. Forces vary only slightly with cutting speed. Fig. 22 shows their dependence on  $h$ . With infinite cut-off strain, simulated forces are upper bounds to experiments. With cut-off strain reducing with temperature, both with and without pre-strain, they are lower bounds. Temperature results for all  $h$  and  $v_c$  are unified by plotting  $\Delta T$  relative to  $F_C^*$  against  $h v_c$ . This is shown in Fig. 23. As simulation conditions change from no cut-off strain, to cut-off strain reducing with temperature, to including a pre-strain, simulated  $\Delta T/F_C^*$  and its rate of change with  $h v_c$  increase. The best fit to the simulations including pre-strain is parallel to and systematically greater than the experimental results by  $\approx 70$  °C/GPa. A difference of this magnitude is expected as the experiment measures the temperature at the tool side face (Section 2.3) while the simulation gives the temperature at the chip mid-section (Arrazola et al., 2015). (The physical basis for plotting results as in Fig. 23 is that temperature rise is expected to be in proportion to work per volume, or  $F_C^*$ , other things being equal, and the partition of heat between work, chip and tool. The latter depends on the Peclet number  $h v_c / \kappa$ , with  $\kappa$  the thermal diffusivity of the work material, and on the ratio of tool to work thermal conductivity. For a fixed tool and work material, the variables are  $F_C^*$  and  $h v_c$ .)

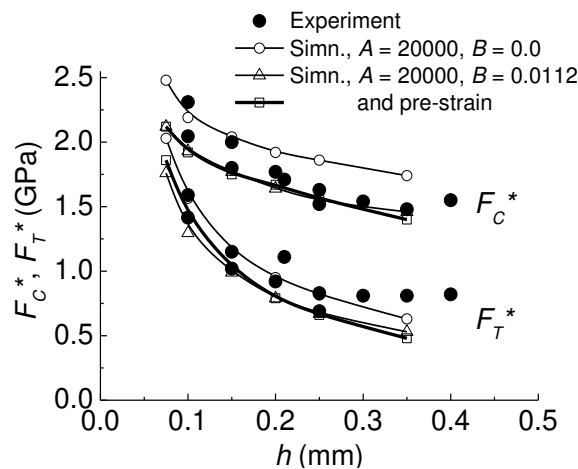


**Fig. 22.** Comparisons of experimental and simulated dependencies on  $h$  of cutting and thrust forces  $F_C^*$  and  $F_T^*$ , in higher speed cutting conditions.

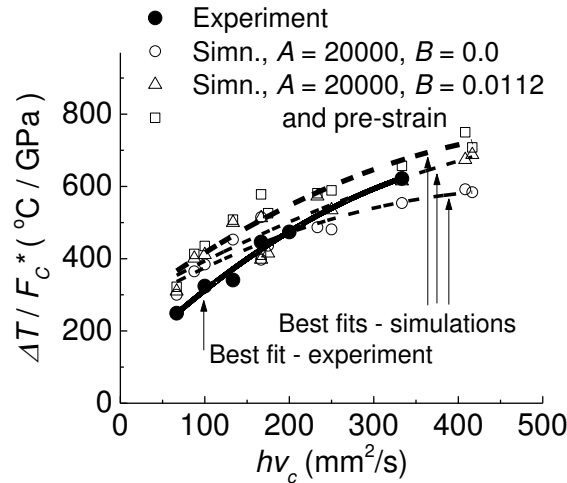


**Fig. 23.** Comparisons of experimental and simulated dependencies on  $h v_c$  of maximum tool temperature rise  $\Delta T$  relative to  $F_c^*$ , in higher speed cutting conditions.

## 7. Discussion

This paper's underlying assumption is that the work material flow stress and failure behaviour determines the shear stresses in both the primary (chip forming) and secondary (chip / tool friction) deformation zones. Friction cannot be adjusted independently of the flow and failure behaviour.

Within this constraint, a flow stress equation without strain softening, when combined with the proposed failure law, leads to predicted tool forces and maximum temperatures close to those measured experimentally. Chip serration is also predicted but maximum and minimum thicknesses of the serrations are too large. Two additions to the model improve the predictions of chip serration as well as of tool forces and temperatures.

The first is to include a small strain softening in the flow stress model, namely that the cut-off strain, the strain at which strain hardening ceases, reduces as temperature increases (Eq. 6). Improved agreement between simulation and experiment is obtained when it is imposed that the cut-off strain reduces to values that occur during chip formation as temperature increases above  $700^\circ\text{C}$ . These temperatures occur in the secondary shear, not the

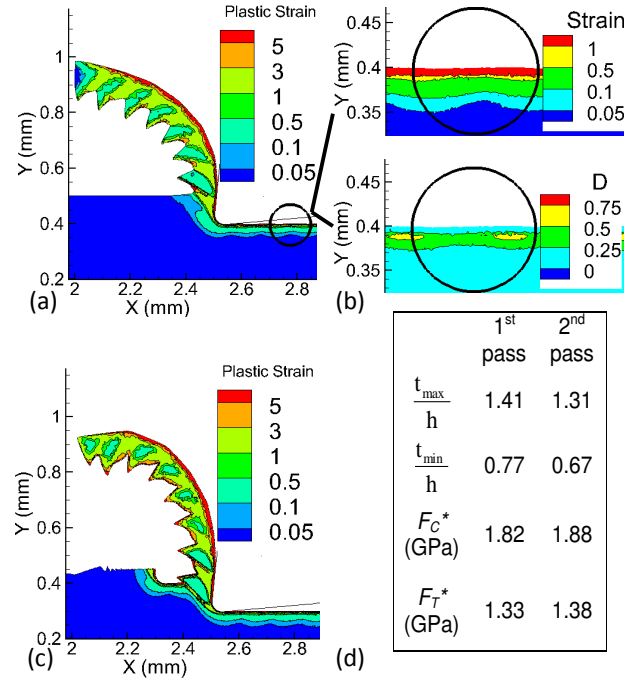
primary shear, zone (Fig. 13d). The strain softening is occurring to reduce the friction stress between chip and tool. It is not acting to alter the flow stress (already reduced by damage, Eq. 8) within the localised shear region of chip serration, as is its purpose in models that propose large strain softening to explain chip serration.

The second is to suppose a pre-strain of 0.1 to exist in the work. In Section 6 it is speculated that this is a proxy for the real damaged and strained state of the cut surface from the previous pass of the tool. This is considered further next.

### 7.1. Damage and strain in the cut surface

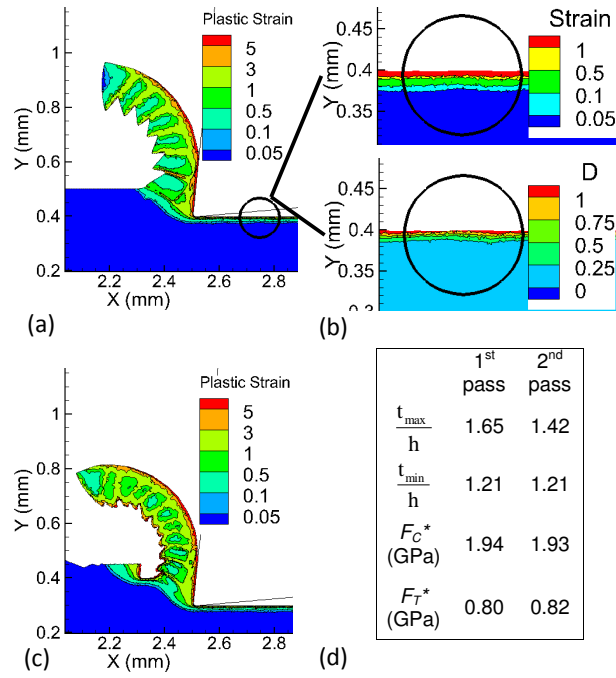
Two simulations are reported here in which the tool passes twice over the cut surface. On the first pass there is no pre-strain in the surface. The second pass experiences the damage and strain hardening from the first pass. It is found that the second pass chip formation is similar to single pass chip formation with pre-strain in the surface.

Fig. 24 is for the example from Fig. 21 of  $h = 0.1$  mm,  $v_c = 100$  m/min, with the initial work material condition  $A = 20,000$  and  $B = 0.0112$  and no pre-strain. Part (a) shows the first pass chip formation, (b) a detail of the sub-surface strain and damage profile, (c) the second pass chip formation and (d) quantitative differences between the passes. (d) records that  $t_{\max}/h$  and  $t_{\min}/h$  are reduced from the first to the second pass in the same way that pre-strain reduces these in Fig. 21. It also records 3 to 4% increases in  $F_C^*$  and  $F_T^*$  from the first to second pass. These changes are insignificant as far as agreement with experiments are concerned (Fig. 22).



**Fig. 24.** Sub-surface strain and damage influences,  $h = 0.1$  mm,  $v_c = 100$  m/min,  $r_\beta = 35$   $\mu$ m: (a) 1<sup>st</sup> pass chip formation, (b) strain and damage in the cut surface, (c) 2<sup>nd</sup> pass chip formation, (d) quantitative differences. (Cut distance = 0.8 mm.)

If the previous pass influences chip formation, the low speed failure model validation simulations should be re-visited. Fig. 25 repeats Fig. 24 but for the example  $h = 0.1$  mm and  $v_c = 10$  m/min, with the model flow and failure coefficients as in Figs. 18, 19, with  $\varepsilon_{f,0} = 0.25$ ,  $c = -1.5$ . In this case,  $t_{\min}/h$ ,  $F_C^*$  and  $F_T^*$  remain unchanged (part c) but  $t_{\max}/h$  is significantly reduced to below its measured value. On the other hand the serration pitch is reduced by  $\approx 40\%$  from the first to the second pass (from counting the number of serrations in the cut distance in parts a and c), bringing that closer to the experimental state (Fig. 19). The validation remains imperfect but not weakened by considering the previous pass effect.



**Fig. 25.** Sub-surface strain and damage influences,  $h = 0.1$  mm,  $v_c = 10$  m/min,  $r_\beta = 10$   $\mu$ m: (a) 1<sup>st</sup> pass chip formation, (b) strain and damage in the cut surface, (c) 2<sup>nd</sup> pass chip formation, (d) quantitative differences. (Cut distance = 0.8 mm.)

The different responses shown in Figs. 24 and 25 of chip formation to deformation and damage from the previous pass arise from the different damage profiles. In Fig. 24, although the tool of 35  $\mu$ m edge radius causes deformation and damage to a depth  $\approx 50$   $\mu$ m, the maximum value of  $D$  occurs below the surface and is less than 1. At the surface, healing reduces  $D$  to zero. In Fig. 25, the sharper tool (10  $\mu$ m edge radius) causes deformation and damage only to a depth  $\approx 20$   $\mu$ m but  $D = 1$  at the surface. These differences might be expected to affect the machined surface integrity.

There is a need to determine experimentally whether the cut surface state is as predicted. Fig. 26 is a longitudinal section of a surface cut at  $v_c = 3$  m/min,  $h = 0.1$  mm, with a tool of edge radius 10  $\mu$ m. It is etched to show grain boundaries. There is a surface layer approximately 10  $\mu$ m thick in which the boundaries are clearly dragged in the direction of tool travel. The arrow points to an example. Superimposed to the right is the simulated depth dependence of strain from Fig. 25b. At the depth of 10  $\mu$ m the strain is  $\approx 0.4$ . At 20  $\mu$ m it is

negligible. These dimensions match the experimental observation. The simulation also predicts a boundary, at a depth of  $\approx 3 \mu\text{m}$ , above which  $D = 1$ . Strain rises rapidly from this boundary to reach  $\approx 7$  at the cut surface. How realistic this is, in terms of strain magnitude or the nature of any damage, is not clear from the section to the left. Work, including extending to studies of surface integrity, is beyond the scope of this paper and remains to be done.

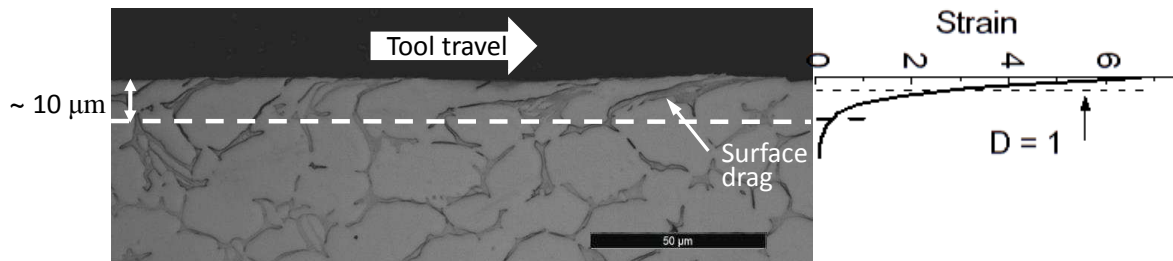


**Fig. 26.** (left) a longitudinal section through a surface cut at  $h = 0.1 \text{ mm}$ ,  $v_c = 3 \text{ m/min}$  and (right) the simulated strain depth distribution from Fig. 25b.

## 7.2. Cutting edge radius influence on cutting and thrust force

Figs. 24d and 25d record different sizes of  $F_T^*$ . This is mainly a tool sharpness (ploughing) effect, though there is a small contribution from their different cutting speeds. It is well established that tool edge radius influences thrust force more than cutting force, as comprehensively reviewed in (Denkena and Biermann, 2014). Fig. 27 presents this work's predictions of  $F_C^*$  and  $F_T^*$  dependence on  $h$  for the low speed tests (Section 5) for which  $r_\beta = 10 \mu\text{m}$ . It includes simulated results for  $v_c = 10$  and  $100 \text{ m/min}$  as well as the experimental results over the speed range 1 to  $10 \text{ m/min}$ . It complements the higher speed data in Fig. 22. It shows an agreement between the experiments and  $v_c = 10 \text{ m/min}$  simulations. The small (predicted) influence of cutting speed on  $F_C^*$  and  $F_T^*$  is seen by comparing the simulation results for  $v_c = 10$  and  $100 \text{ m/min}$ . A comparison with Fig. 22 shows  $F_C^*$  to be almost unchanged between the two but  $F_T^*$  to be much reduced, the more so the smaller is  $h$ . It confirms the major influence of edge radius on  $F_T^*$ .

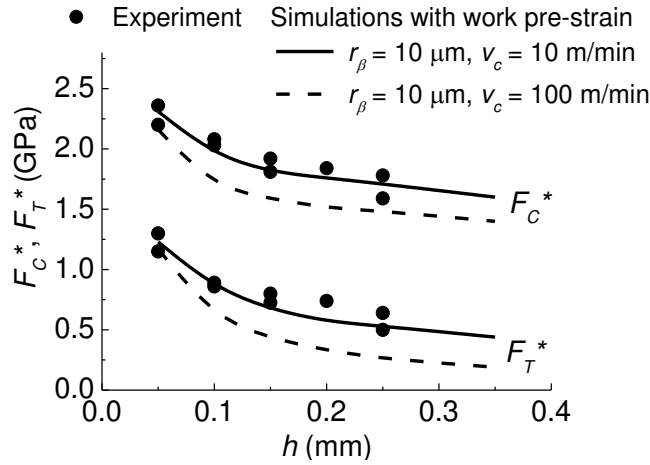


Fig. 27. Comparisons of experimental and simulated dependencies on  $h$  of cutting and thrust forces  $F_C^*$  and  $F_T^*$ , in low speed cutting conditions.

The different dependences of  $F_C^*$  and  $F_T^*$  on  $h$  and to a lesser extent on  $v_c$  lead to the ratio  $F_T^*/F_C^*$  varying with  $h$  and  $v_c$ . Consequently the ratio of friction force to normal force on the tool face also varies with  $h$  and  $v_c$ . This ratio is called here the effective friction coefficient,  $\mu_{\text{effective}}$ , to distinguish it from  $\mu$ , the input to the simulations (Eq. 9). Fig. 28 shows the simulated dependencies of  $\mu_{\text{effective}}$  on  $h$  for different levels of  $v_c$ , and also compares these with values in the literature.

Fig. 28a includes the values assumed in simulations for  $r_\beta = 10 \mu\text{m}$  in (Melkote et al., 2015) to obtain agreement with experiments (as referenced in Section 1). Fig. 28b includes experimental values at  $v_c = 70 \text{ m/min}$  from measured cutting and thrust forces in (Wyen and Wegener, 2010). In both cases the trends from the present and previous works are the same but the present work underestimates the previous values. In the case of Fig. 28a the reason may simply be that the values in Melkote et al. are chosen to give agreement between that paper's simulations and experiments, and that paper's model is different from the present one. In the case of Fig. 28b the reason is in part the different rake angles involved,  $\gamma = 6^\circ$  in the present work and  $10^\circ$  in Wyen and Wegener. The present work's  $\mu_{\text{effective}}$  values are  $\approx 0.1$

less than from Wyen and Wegener. In a trial simulation at  $v_c = 100$  m/min,  $h = 0.1$  mm,  $\mu_{\text{effective}}$  is increased by 0.05 by changing  $\gamma$  from 6 to 10°.

Rather than being concerned by small differences in  $\mu_{\text{effective}}$  between this and previous works, the more important point is that all the values of  $\mu_{\text{effective}}$  in this work are consequences of the single friction law, Eq. 9, with  $\mu = 1.0$ . Values of  $\mu_{\text{effective}}$  come naturally from first the tool edge radius and uncut chip thickness, then the flow stress of the chip material next to the rake face (the speed effect) and finally perhaps a small amount also from the rake angle.

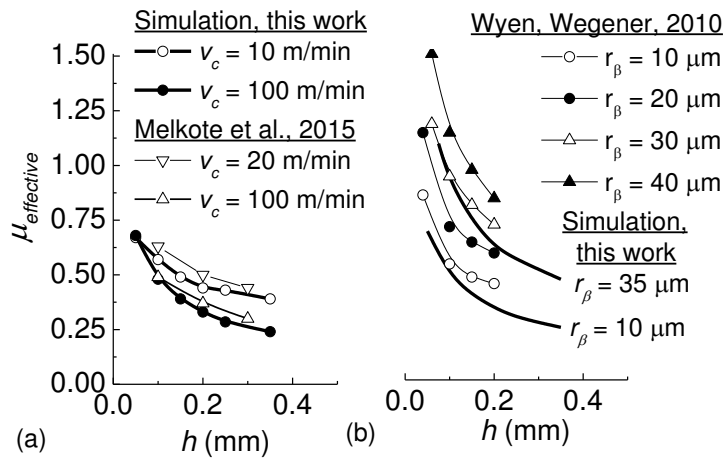


**Fig. 28.** Dependencies of  $\mu_{\text{effective}}$  on  $h$ : (a) this work's simulations for  $r_\beta = 10$   $\mu\text{m}$  and  $v_c = 10$  and 100 m/min compared to assumed simulation input values in (Melkote et al., 2015); (b) this work's simulations at higher speed for  $r_\beta = 10$  and 35  $\mu\text{m}$  compared to experimentally measured values in (Wyen and Wegener, 2010).  $\mu_{\text{effective}}$  is the ratio of friction to normal force from resolving cutting and thrust force parallel and normal to the tool rake face.

### 7.3. The failure model

The main innovation of this work is the failure model. The failed flow stress in compression is a fraction of the unfailed stress that depends on the (negative) stress triaxiality and the temperature. It has only two parameters (Eq. 8): an internal friction coefficient  $\mu_i = 1$  and a healing temperature range of 600 to 700°C. In previous work on built up edge prediction, in which the present model without healing is applied,  $\mu_i = 0.9$  was used (Childs, 2013). Fig. 14 shows there is only a small sensitivity of chip formation to  $\mu_i$  in the range  $\mu_i =$

0.9 to 1. The temperature range 600 to 700°C is the range over which the homologous temperature increases through half the melting temperature.

In addition to the failure model, a model is needed for the onset of failure. A simple accumulation of damage  $D$  up to a value  $D = 1$  is used, with an exponential dependence of damage increment on stress triaxiality (Eqs. 1, 7): parameters of the model that give good agreements with experiment are  $\varepsilon_{f,0} = 0.25$  to  $0.3$ ,  $c = -1.0$  to  $-1.5$  and  $a = 0.0012$ . These values are within the ranges of values determined from non-machining tests.

These damage accumulation and failure models have a simple physical interpretation. This and their small number of coefficients makes them, in the present authors' views, easy and robust to use over a wide range of cutting speeds and uncut chip thicknesses. They differ fundamentally from the existing strain softening models that are reviewed in Section 1. First of all the development of damage and the damaged flow stress relative to its undamaged value depend on pressure and temperature (through Eqs. 1, 7, 8) and not on strain (and strain rate) and temperature. The pressure dependence leads to changes of predicted chip formation with cutting speed that are fully described in Section 4 around Figs. 12 and 13. Secondly, in adiabatic conditions (this paper's higher speed conditions), damage acts primarily to trigger instability. As temperature in the deforming regions increases the flow stress reduces due to the heating but the additional fractional reduction due to damage decreases. This is the opposite of behaviour in strain softening models, for example Calamaz (2010), in which the additional fractional reduction due to strain softening increases with temperature.

It is a strength of the models that they are applied successfully with a constant set of coefficients over the full range of speeds and uncut chip thicknesses. However the coefficient values are obtained from matching simulation and experimental results at low cutting speed. If two pass instead of single pass simulations had been chosen, as in Fig. 25, a slightly different set of best fit values might have emerged (a complete set of two pass simulations at

low speed is not practicable due to the large elapsed computing times needed). There is a need for independent shear damage and failure testing in the compressive conditions of machining, i.e. at stress triaxialities down to  $-0.8$ .

#### 7.4 Flow stress model uncertainties

In the Introduction, several secondary reasons for the work are listed. One is reducing uncertainties by carrying out the model parameter determination and machining experiments on the same stock of work material. Fig. 6 gives the present work materials' room temperature, low strain rate, strain hardening behaviour while Figs. 5 to 7 show its strain hardening, thermal softening and strain rate hardening relative to other results from the literature. From these observations lower bound strain hardening and thermal softening and upper bound strain rate hardening coefficients are applied to the simulations.

It could also be asked what uncertainty arises from the choice of test methods for determining the coefficients, namely room temperature low strain rate testing for strain hardening and hydraulic testing for temperature and strain rate dependence. An implication of the product form of flow stress equation, Eq. 2, is that strain and strain rate hardening, and thermal softening, are independent of each other. For this to apply at least the plastic flow mechanism should be unchanged by changes in temperature and strain rate. Data exists for titanium that the boundary between obstacle controlled plasticity and power law creep occurs at a strain rate  $\approx 10^{-6}/s$  at  $20^{\circ}C$ ,  $\approx 100/s$  at  $400^{\circ}C$ , rising to  $\approx 10^3/s$  at  $800^{\circ}C$  (Frost and Ashby, 1982). If these values also apply to Ti6Al4V then the room temperature, low strain rate, strain hardening testing is applicable to machining conditions (falling within the obstacle controlled plasticity range) but the hydraulic testing (Table 2 conditions) falls increasingly outside machining conditions as temperature increases above  $400^{\circ}C$  (becoming power law creep

determined). This is seen in the results of Figs. 6 and 7. It makes the simulations' choice of thermal softening and strain rate hardening coefficients uncertain.

For these reasons, simulations (not reported in detail) have been carried out with inputs as for the  $A = 20,000$ ,  $B = 0.0112$  simulations of Figs. 21 to 23 except for applying the mid-range flow stress coefficients from Table 3, though not varying  $\sigma_0$  from 930 MPa.  $F_C^*$  and  $F_T^*$  are increased by  $\approx 3\%$ , tool temperature rise by  $\approx 5\%$  and  $t_{\max}/h$  and  $t_{\min}/h$  by  $\approx 10\%$ . These are the levels of uncertainty in the present work from uncertainty in flow stress coefficients.

### 7.5. Roles of the coefficients

A further secondary reason is implementing a model with a small number of coefficients such that their role is clear. This reason has already been addressed in part in this discussion, as far as coefficients of the damage and failure models are concerned. More broadly, the strain hardening and thermal softening of the flow stress model, and to a lesser extent the strain rate hardening, together with the input machining conditions, determine the strain and hydrostatic stress fields in which damage accumulates. The flow stress and damage accumulation models thus control the instant at which  $D$  reaches 1. The consequent drop in flow stress acts as a trigger to initiate flow instability, in addition to the thermal softening. These therefore determine  $t_{\max}/h$ . Once the instability has started, it continues (and determines  $t_{\min}/h$ ) by an amount dominated by the dependence of failed flow stress on pressure (in low speed conditions) or by further softening due to adiabatic heating (in high speed conditions).

## 7.6. Final comments

The focus of this paper is the development of the flow and failure model and its testing against experimental results. The model's practical value is as input to simulations of metal cutting chip formation, in this case of annealed Ti6Al4V, for predicting tool mechanical and thermal loading, as in Figs. 22 and 23. In particular, Fig. 23 shows that tool temperature rise can be predicted from measurement of specific cutting force and the existing uncut chip thickness and cutting speed. Simulations with other tool geometries and other tool thermal conductivities would generate different trajectories.

Finally, this paper takes annealed Ti6Al4V as its work material because of its long history of study. There is much published work on its flow stress dependence on strain, strain rate and temperature; and even some on its ductile shear failure behaviour. The same arguments about the importance of thermal instability, strain softening and failure in triggering serrated chip formation, that are the focus of this paper, also occur for other alloy systems. For example (Poulachon et al., 2001) explain transitions from continuous to serrated chip formation in machining 100Cr6 steel, that depend on the hardness of the steel, entirely by applying Recht's (1964) instability criterion. Rhim and Oh (2006) invoke strain softening to account for serration in AISI 1045 steel machining. Lorentzen et al. (2009) show the need to include damage in simulating Inconel 718 machining. An ambition is to extend the present work to these other alloys. However, except for annealed carbon steels, there is only limited information available on the shear failure of these alloys with heat treatments relevant to machining, in particular in compressive conditions. Lack of data on compressive shear failure in other alloy systems is the main barrier to a wider application of the present work. It might also be that modelling the thermal softening when a phase change occurs in the shear localised region is more difficult than when it does not. No such change occurs in the present

work (Figs. 1 and 20) but a phase change is well-known to occur in machining hardened steels and also occurs in some Ti alloys more readily than in Ti6Al4V (Germain et al., 2013).

## **8. Summary and conclusions**

A combined flow stress and failure model for annealed Ti6Al4V has been developed and applied to simulation of chip formation over the cutting speed range 1 to 100 m/min and at uncut chip thicknesses from 0.1 to 0.35 mm. It gives agreement with experimental measurements of specific cutting and thrust forces, maximum tool temperatures and chip geometries over the same range of cutting conditions.

The flow stress model is of power law form, with coefficients determined from mechanical testing. It does not include the large strain softening behaviour proposed in some recent works to account for observed saw tooth chip formation. It does include a small strain softening. A critical strain is imposed above which strain hardening ceases. This critical strain reduces with increasing temperature, from  $\approx 10$  at 700°C to  $\approx 0.3$  at 1000°C. The consequent flow stress reduction acts to reduce the friction stress between chip and tool at high cutting speeds rather than to ease flow in the saw tooth shear bands.

The failure model supposes damage  $D$  to increase with strain increment along a stream line in a standard way, with an inverse exponential dependence on stress triaxiality. The exponential coefficient and pre-exponential factor are given values from the ductile shear failure literature for Ti6Al4V. Failure occurs when  $D$  reaches 1. The paper's novel feature is that the failed flow stress is taken to be a fraction of the unfailed value that, at low (negative) stress triaxiality, is in proportion to the triaxiality. At high negative triaxiality the failed flow stress regains its unfailed value. Also failure heals as the temperature increases through the range 600 to 700°C, i.e. to above half the melting temperature measured in Kelvin.

The failure model, with its coefficients, is validated by comparing simulated and experimental cutting test results at low cutting speeds (1 to 10 m/min) when adiabatic shear does not occur. It is this validated model that then also gives agreements between simulated and experimental cutting and thrust forces and tool temperatures at high cutting speeds. To obtain agreement as far as maximum and minimum thicknesses of the chip saw teeth are concerned it is necessary to consider the surface strain and damage in the work material caused by the previous pass of the tool.

The applied value of the work is in its results for tool mechanical and thermal loading, and the modelling that could be applied to other machining conditions and to the machining of other materials, provided that the model's coefficients are available for those materials.

### **Acknowledgements**

Modelling and simulation was carried out at the University of Leeds and did not receive any specific grant from funding agencies in the public, commercial or not-for-profit sectors. Most of the experimental work was carried out at Mondragon University, with funding for staff and equipment time from the Basque and Spanish Government projects respectively MICROMAQUINTE (PI\_2014\_1\_116) and EMULATE (DP12015-67667-C3-3R). Work materials were provided by TIMET and Aubert and Duval and tool materials by Sandvik. The hydraulic mechanical (Gleeble) testing was carried out at Ecole Nationale Supérieure d'Arts et Métiers (ENSAM) d'Angers: we thank Guenaël Germain and Eliane Giraud for making this available and for their guidance.

## References

- Allahverdizadeh, N., Gilioli, A., Manes, A., Giglio, M., 2015. An experimental and numerical study for the damage characterization of a Ti6Al4V titanium alloy. *International Journal of Mechanical Sciences* 93, 32-47.
- Arrazola, P.J., Aristimuno, P., Soler, D., Childs, T.H.C., 2015. Metal cutting experiments and modelling for improved determination of contact temperature by infrared thermography. *CIRP Annals – Manufacturing Technology* 64/1, 57-60.
- Armendia, M., Garay, A., Villar, A., Davies, M.A., Arrazola, P.J., 2010. High bandwidth temperature measurement in interrupted cutting of difficult to machine materials. *CIRP Annals – Manufacturing Technology* 59/1, 97-100.
- ASTM E112-13, 2013. Standard Test Methods for Determining Average Grain Size, ASTM International, Westconshohcken, doi:10.1520/E0112.
- Bai, Y., Wierzbicki, T., 2010. Application of extended Mohr-Coulomb criterion to ductile fracture. *International Journal of Fracture* 161, 1-20.
- Calamaz, M., Coupard, D., Girot, F., 2008. A new material model for 2D numerical simulation of serrated chip formation when machining titanium alloy Ti6Al4V. *International Journal of Machine Tools and Manufacture* 48, 275-288.
- Calamaz, M., Coupard, D., Girot, F., 2010. Numerical simulation of titanium alloy dry machining with a strain softening constitutive law. *Machining Science and Technology* 14, 244-257.
- Chen, G., Ren, C., Yang, X., Jin, X., Guo, T., 2011. Finite element simulation of high-speed machining of titanium alloy (Ti6Al4V) based on ductile failure model. *International Journal of Advanced Manufacturing Technology* 56, 1027-1038.
- Childs, T.H.C., 2013. Ductile shear failure damage modelling and predicting built-up edge in steel machining. *Journal of Materials Processing Technology* 213, 1954-1969.

Childs, T.H.C., 2014. Adiabatic shear in metal machining. In: CIRP Encyclopedia of Production Engineering. Eds. Laperriere L, Reinhart G. Springer Reference, Berlin, pp.27-33.

Childs, T.H.C., Rahmad, R., 2010. Modifying strain-hardening of carbon steels for improved finite element simulation of orthogonal machining. Proceedings of the Institution of Mechanical Engineers, Pt. B Journal of Engineering Manufacture 224B, 721-732.

Childs, T.H.C., Otieno, A.W., 2012. Simulations and experiments on machining carbon and low alloy steels at rake face temperatures up to 1200°C. Machining Science and Technology 16, 96-110.

Denkena, B., Biermann, D., 2014. Cutting edge geometries. CIRP Annals – Manufacturing Technology 63/2, 631-653.

El-Magd, E., Treppmann, C., Korthauer, M., 2005. Experimentelle und numerische Untersuchung zum thermomechanischen Stoffverhalten. In Tonshof HK, Hollmann F (eds.) Hochgeschwindigkeitsspanen metallischer Werkstoffe, Wiley\_VCH Verlag, Weinheim, pp.183-206.

Follansbee, P.S., Gray III, G.T., 1989. An analysis of the low temperature, low and high strain-rate deformation of Ti-6Al-4V. Metallurgical Transactions 20A, 863-874.

Frost, H.J., Ashby, M.F., 1982. Deformation-Mechanism Maps. Pergamon Press, Oxford, Ch. 17.2.

Germain, G., Morel, A., Braham-Bouchnak, T., 2013. Identification of material constitutive laws representative of machining conditions for two titanium alloys:Ti6Al4V and Ti555-3. Journal of Engineering Materials and Technology 135, 031002-1 to 11.

Hammer, J.T., 2012. Plastic Deformation and Ductile Fracture of Ti6Al4V Under Various Loading Conditions. MSc thesis, Department of Mechanical Engineering, The Ohio State University.

Hou, Z.B., Komanduri, R., 1997. Modeling of thermomechanical shear instability in machining. *International Journal of Mechanical Sciences* 39, 1273-1314.

Iturbe, A., Giraud, E., Hormaetxe, E., Garay, A., Germain, G., Ostolza, K., Arrazola, P.J., 2017. Mechanical characterisation and modelling of Inconel 718 material behaviour for machining process assessment. *Materials Science and Engineering A* 682, 441-453.

Johnson, G.R., Cook, W.H., 1985. Fracture characteristics of three metals subjected to various strains, strain rates, temperatures and pressures. *Engineering Fracture Mechanics* 21, 31-48.

Johnson, G.R., Holmquist, T.J., 1989. Test data and computational strength and fracture model constants for 23 materials subjected to large strain, high strain rates and high temperatures. Los Alamos National Laboratory Report LA-11463-MS (Limited access).

Kailas, S.V., Prasad, Y.V.R.K., Biswas, S.K., 1994. Flow instabilities and fracture in Ti6Al4V deformed in compression at 298K to 673K. *Metallurgical and Materials Transactions* 25A, 2173-2179.

Khan, A.S., Suh, Y.S., Kazmi, R., 2004. Quasi static and dynamic loading responses and constitutive modelling of titanium alloys. *International Journal of Plasticity* 20, 2233-2248.

Khan, A.S., Kazmi, R., Farrokh, B., Zupan, M., 2007. Effect of oxygen content and microstructure on the thermos-mechanical response of three Ti6Al4V alloys: experiments and modelling over a wide range of strain-rates and temperatures. *International Journal of Plasticity* 23, 1105-1125.

Komanduri, R, von Turkovich, B.F., 1981. New observations on the mechanism of chip formation when machining titanium alloys. *Wear* 69, 179-188.

Lee, W.-S., Lin, C.-F., 1998. Plastic deformation and fracture of Ti-6Al-4V alloy loaded with high strain rate under various temperatures. *Materials Science and Engineering A* 241, 48-59.

Liu, J., Bai, Y., Xu, C., 2014. Evaluation of ductile fracture models in finite element simulation of metal cutting processes. *Journal of Manufacturing Science and Engineering* 136, 011010-1-14.

Liu, R., Melkote, S., Pucha, R., Morehouse, J., Man, X., Marusich, T., 2013. An enhanced constitutive material model for machining of Ti6Al4V alloy. *Journal of Materials Processing Technology* 213, 2238-2246.

Lorentzon, J., Jarvstrat, N., Josefson, B.L. 2009. Modelling chip formation of alloy 718. *Journal of Materials Processing Technology* 209, 4645-4653.

Macdougall, D.A.S., Harding, J., 1999. A constitutive relation and failure criterion for Ti6Al4V alloy at impact rates of strain. *Journal of the Mechanics and Physics of Solids* 47, 1157-1185.

Melkote, S.N., Liu, R., Fernandez-Zelaia, P., Marusich, T., 2015. A physically based constitutive model for simulation of segmented chip formation in orthogonal cutting of commercially pure titanium. *CIRP Annals – Manufacturing Technology* 64, 65-68.

Marusich, T.D., Ortiz, M., 1995. Modelling and simulation of high-speed machining. *International Journal for Numerical Methods in Engineering* 38, 3675-3694.

Mondelin, A., Valiorgue, F., Feulvarch, E., Rech, J., Coret, M., 2013. Calibration of the insert/tool holder thermal contact resistance in stationary 3D turning. *Applied Thermal Engineering* 55, 17-25.

Nemat-Nasser, S., Guo, W., Nesterenko, V.F., Indrakenti, S.S., Gu, Y., 2001. Dynamic response of conventional and hot isostatically pressed Ti6Al4V alloys: experiments and modelling. *Mechanics of Materials* 33, 425-439.

Oxley, P.L.B., 1989. *Mechanics of Machining*. Ellis Horwood, Chichester, Ch. 4.

Poulachon, G., Moisan, A., Jawahir, S. 2001. Modelling the influence of thermo-mechanical behaviour in chip formation during hard turning of 100Cr6 bearing steel. *CIRP Annals – Manufacturing Technology* 50/1, 31-36.

Recht, R.F., 1964. Catastrophic thermoplastic shear. *Transactions of ASME Journal of Applied Mechanics* 31, 189-193.

Rhim, S.-H., Oh, S.-K. 2006. Prediction of serrated chip formation in metal cutting process with new flow stress model for AISI 1045 steel. *Journal of Materials Processing Technology* 171, 417-422.

Semiatin, S.L., Rao, S.B., 1983. Shear localization in metal cutting. *Materials Science and Engineering* 61, 185-192.

Simha, C.H.J., Williams, B.W., 2016. Modeling failure of Ti6Al4V using damage mechanics incorporating effects of anisotropy, rate and temperature on strength. *International Journal of Fracture* 198, 101:115.

Seo, S., Min, O., Yang, H., 2005. Constitutive equation for Ti6Al4V at high temperatures measured using the SHPB technique. *International Journal of Impact Engineering* 31, 735-754.

Usui, E., Obikawa, T., Shirakashi, S., 1984. Study on chip segmentation in machining titanium alloy: In Proc. 5<sup>th</sup>. Int. Conf. on Production Engineering, Tokyo 9-11 July, pp. 233-239.

Vyas, A., Shaw, M.C., 1999. Mechanics of saw-tooth chip formation in metal cutting. *Journal of Manufacturing Science and Engineering* 121, 163-172.

Wyen, C.-F., Wegener, K., 2010. Influence of cutting edge radius on cutting forces in machining titanium. *CIRP Annals – Manufacturing Technology* 59/1, 93-96.

Zerilli, F.J., Armstrong, R.W., 1987. Dislocation mechanics based constitutive relations for material dynamics calculations. *Journal of Applied Physics* 61, 1816:1825